

2021-05-01

Geotechnical Aspects Of Martian Regolith Simulant Jsc Mars-1

Jesus Baca
University of Texas at El Paso

Follow this and additional works at: https://scholarworks.utep.edu/open_etd



Part of the [Civil Engineering Commons](#)

Recommended Citation

Baca, Jesus, "Geotechnical Aspects Of Martian Regolith Simulant Jsc Mars-1" (2021). *Open Access Theses & Dissertations*. 3220.

https://scholarworks.utep.edu/open_etd/3220

This is brought to you for free and open access by ScholarWorks@UTEP. It has been accepted for inclusion in Open Access Theses & Dissertations by an authorized administrator of ScholarWorks@UTEP. For more information, please contact lweber@utep.edu.

GEOTECHNICAL ASPECTS OF MARTIAN REGOLITH SIMULANT JSC MARS-1

JESUS BACA

Master's Program in Civil Engineering

APPROVED:

Reza Ashtiani, Ph.D., P.E., Chair

Jose M. Hurtado, Jr., Ph.D.

Carlos M. Ferregut, Ph.D.

Stephen L. Crites, Jr., Ph.D.
Dean of the Graduate School

Copyright ©

by

Jesus Baca

2021

DEDICATION

I dedicate this thesis to my academic mentor, Reza Ashtiani, Ph.D., P.E., I am grateful for your wisdom, knowledge, and the opportunity of being your student research assistant for more than 3 years. To my industry mentor, Bernardino Olague, P.E., PMP, thank you for all your support, for your patience, and for motivating me to become a better engineer. To my mother, Carmen Ramirez, thank you for always believing in me. To my friend, German Garay, thank your unconditional support and advices.

GEOTECHNICAL ASPECTS OF MARTIAN REGOLITH SIMULANT JSC MARS-1

by

JESUS BACA, BSCE, EIT

THESIS

Presented to the Faculty of the Graduate School of

The University of Texas at El Paso

in Partial Fulfillment

of the Requirements

for the Degree of

MASTER OF SCIENCE

Department of Civil Engineering

THE UNIVERSITY OF TEXAS AT EL PASO

May 2021

ACKNOWLEDGEMENTS

I would like to express my sincere gratitude to my graduate advisor and committee chairman, Dr. Reza Ashtiani, P.E., for his guidance, support, patience, and mentorship. His passion and dedication for mentoring and sharing his knowledge is exceptionally inspirational for me.

Moreover, I would also like to acknowledge the assistance and support from my colleagues and peers, Edgar Rodriguez, Jacob Wessel, Ali Morovatdar, Arash Karimi Pour, Alan Quiñonez, Mohammed Rashidi, German Garay, Hector Cruz, Carlos Licon, and Margarita Ordaz.

ABSTRACT

The primary objective of this research was to mechanistically characterize the physical and mechanical properties of the JSC Mars-1 regolith simulant to better understand its physical, mechanical, and physio-chemical properties. JSC Mars-1 is a regolith simulant developed by the National Aeronautics and Space Administration (NASA) at the Johnson Space Center (JSC) based on the data collected by instruments on the Viking and the Pathfinder landers. A comprehensive experiment matrix was devised to simulate the extraterrestrial compaction characteristics of unbound simulants in the laboratory. The resilient properties, strength parameters, and deformation potential were of primary interest in this effort. In addition, the influence that the chemical composition of JSC Mars-1 has in its mechanical properties was also studied. For this, the strength and deformation potential of the JSC-1 Mars-1 were contrasted with limestone materials collected from El Paso, Texas. The study also investigated the contribution of the magnitude and method of application of the compaction energy on the dilatancy of particulate materials in the laboratory. The laboratory experiments showed significant strain rate dependency of the strength parameters for simulants at multiple relative compaction levels. This underscores the significance of nonlinear and anisotropic regolith modeling for the proper determination of orthogonal strength, deformation potential, and stability of platforms.

TABLE OF CONTENTS

DEDICATION.....	III
ACKNOWLEDGEMENTS.....	V
ABSTRACT.....	VI
TABLE OF CONTENTS.....	VII
LIST OF TABLES.....	IX
LIST OF FIGURES.....	X
CHAPTER 1: INTRODUCTION.....	2
1.1 Objectives.....	2
1.2 Organization.....	5
CHAPTER 2: LITERATURE REVIEW.....	7
2.1 Relating JSC Mars-1 with Martian Native Regolith Materials.....	7
2.1.1 Martian Surface Geological Units and Periods.....	7
2.1.2 Martian Topography.....	10
2.2 Development of JSC Mars-1 Regolith Simulant.....	12
2.3 Loading Conditions and Densification Processes of Martian Regolith.....	15
CHAPTER 3: INDEX PROPERTIES OF JSC MARS-1.....	17
3.1 Particle Size Distribution.....	17
3.2 Characterization of the Fine-grained Particles of JSC Mars-1.....	19
CHAPTER 4: PARTICLE MORPHOLOGY.....	23
4.1 Particle Angularity.....	23
4.2 Particle Sphericity.....	26
CHAPTER 5: ELECTRICAL RESISTIVITY.....	29
CHAPTER 6: DENSITY AND COMPACTION.....	33
6.1 Minimum Index Density.....	34

6.2 Impact Compaction: Modified Effort	34
6.3 Vibratory Compaction	36
6.4 Gyrotory Compaction.....	39
6.5 Comparison of Compaction Methods	42
CHAPTER 7: MECHANICAL PROPERTIES OF JSC MARS-1.....	47
7.1 Input Parameters	47
7.2 Compressibility.....	47
7.3 Shear Strength.....	52
7.4 Dilation Behavior.....	60
CHAPTER 8: IMPACT OF PARTICLE MORPHOLOGY.....	66
8.1 Development of EP-Limesone as an Alternative Simulant	66
8.2 JSC Mars-1 vs EP-Limestone: Physical Properties	68
8.3 JSC Mars-1 vs EP Limestone: Particle Morphology	69
8.4.1 Compressibility.....	72
8.5.2 Shear Strength.....	73
8.5.3 dilatancy behavior.....	75
CHAPTER 9: CONCLUSIONS	77
9.1 Key Findings.....	77
9.2 Recommendations for Future Work.....	78
REFERENCES	80
VITA.....	87

LIST OF TABLES

Table 1: Parameters influencing JSC Mars-1 Mechanical Properties.	2
Table 2: Measured Mechanical and Settlement Properties for JSC Mars-1.	3
Table 3: Laboratory Experiment Matrix	4
Table 4: Mean Elevation and slope statistics for Mars geological units associates with Viking 1, Viking 2, and Pathfinder landing sites.....	10
Table 5. Chemical Compositions of Martian Regolith Materials and JSC Mars-1	13
Table 6. JSC Mars-1 Composition by Soil Group	22
Table 7. Particle Size Concentration for a Range of Angularities.....	26
Table 8. Particle Size Concentration for a Range of Sphericity Values.	28
Table 9. Correlation Between Soil Corrosivity and Electrical Resistivity.	29
Table 10: Electrical Resistivity vs. Moisture Content for JSC Mars-1.....	31
Table 11: Summary of Results for Compaction by Vibration Methods.	38
A set of gyratory compaction tests were performed on JSC Mars-1 using various values of G_r and σ_1 . The results are summarized in Table 12.	40
Table 12: Gyratory Compaction Test Results.....	40
Table 13. Variation of Particle Size as a Function of Compaction Method and Associated Factors.....	46
Table 14. 1-Dimensional Compressibility Tests: Summary of Results.....	51
Table 15. Direct Shear Test: Input Parameters	52
Table 16. Shear Strength Properties of JSC Mars-1	57
Table 17. Direct Shear Test: Angles of Dilation.....	65

LIST OF FIGURES

Figure 1. Laboratory Experiment Flow Chart.....	3
Figure 2. Geological Activity as a function of time on Mars (Carr and Head III, 2010). The approximate boundaries of Martian time periods are shown in giga years (Gyr.) (Hartman and Neukum, 2001). Terrestrial time periods are shown at the left-hand side (Head, 2006).....	8
Figure 3. Hesperian Epochs with subject landing sites (Tanaka, et al., 2014)	9
Figure 4. Global Topographic Map of Mars. Color coded by elevation as determined by the Mars Orbital Laser Altimeter (MOLA).....	11
Figure 5. Particle Size Distribution Curve of JSC Mars-1.....	18
Figure 6: Casagrande Plasticity Chart.....	20
Figure 7. Failure to perform the liquid limit test in the Casagrande device due to absence of adhesion forces between the soil particles and the Casagrande cup.....	21
Figure 8. JSC Mars-1 Particles in the AIMS chamber.	23
Figure 9. Characterization of angularity index for JSC-1 Mars using AIMS. (Left) Relationship of AIMS angularity index of individual particles grouped by four sieve standard sizes. (Right) Visual explanation of the Krumbein scale (Krumbein, 1941).	25
Figure 10. Particle sphericity distribution. (Left) Relationship of AIMS sphericity index of individual particles grouped by four sieve standard sizes. (Right) Visual explanation of the Krumbein scale (Krumbein, 1941).	27

Figure 11. Electrical resistivity vs. moisture content for JSC Mars-1.....	30
Figure 12. JSC Mars-1 in the Miller Box prepared at a relative compaction (RC%) of 99% and a moisture content of 34.6%. Note the seepage of water from the specimen, indicating the degree of saturation is 100%.	32
Figure 13. JSC Mars-1 being poured in a calibrated mold by the raining technique.	34
Figure 14. Shake table equipment.....	36
Figure 15. Maximum index density values achieved by vibration at different rheostat capacities, with respect to minimum index density (<i>Dr% min</i>).....	37
Figure 16. Maximum index density values achieved by vibration methods of compaction.....	39
Figure 17. Dry density (kg m^{-3}) of JSC Mars-1 vs gyration rate (RPM).	41
Figure 18: Dry density values of JSC Mars-1 obtained by using different methods of compaction.	43
Figure 19. Particle size distribution curves developed with the material tested under different ASTM compaction standards.....	45
Figure 20. Compression curves (axial effective stress in logarithmic scale) for JSC Mars-1 corresponding to different initial relative densities (expressed as percent relative compaction). 48	
Figure 21. Pneumatic consolidation load frame used for the compressibility testing of JSC Mars-1.....	49
Figure 22. JSC Mars-1 in the consolidation ring.	49

Figure 23. Direct shear test equipment.	53
Figure 24. Mohr-Coulomb failure envelope (top) and shear stress vs. horizontal displacement relationship (bottom) for RC= 99% and SR=7.62 mm/minute.....	54
Figure 25. Mohr-Coulomb failure envelope (top) and shear stress vs. horizontal displacement relationship (bottom) for RC= 91.8% and SR=7.62 mm/minute.....	55
Figure 26. Mohr-Coulomb failure envelope (top) and shear stress vs. horizontal displacement relationship (bottom) for RC= 83.6% and SR=7.62 mm/minute.....	56
Figure 27. Angle of internal friction and strain rate (left) and cohesion and strain rate (right) relationships.	58
Figure 28. Remains of JSC Mars-1 after direct shear test experiment.	59
Figure 29. Vertical deformation vs. horizontal displacement relationship for RC=99.0%, SR=7.62 mm/min.....	61
Figure 30. Vertical deformation vs. horizontal displacement relationship for RC=91.8%, SR=7.62 mm/min.....	62
Figure 31. Vertical deformation vs. horizontal displacement relationship for RC=83.6%, SR=7.62 mm/min.....	62
Figure 33. Vertical deformation vs. horizontal displacement relationship for RC=75.4%, SR=7.62 mm/min.....	63
Figure 34. Angle of dilation vs. normal stress (kPa).	64

Figure 35. Influence of wet sieving on mechanical properties of EP-Limestone. (Left) Compression curves obtained from wet and dry sieving. (Right) Mohr-Coulomb failure envelopes obtained from wet and dry sieving.....	67
Figure 36. Dry (left) and wet (center) sieving of EP-Limestone particles. (Right) Sieved material.	68
Figure 37. (Left) Specific gravity of JSC Mars-1 and EP-Limestone. (Right) Pycnometers containing EP-Limestone and JSC Mars-1 materials.	69
Figure 38. Angularity indices of JSC Mars-1 and EP-Limestone for various particles sizes.....	70
Figure 39. One-dimensional compression curves for JSC Mars-1 and EP-Limestone for relative initial compaction of 99% (left) and 83.6% (right).....	72
Figure 40. Comparison of the cohesion properties of JSC Mars-1 and EP-Limestone.	73
Figure 41. Comparison of the angle of internal friction of JSC Mars-1 and EP-Limestone.	74
Figure 42. Dilation behavior of JSC Mars-1 (left) compared to EP-Limestone (right).....	76

CHAPTER 1: INTRODUCTION

1.1 Objectives

This research aims to develop a mechanistic characterization of the physical and mechanical properties of the JSC Mars-1 regolith simulant. To date, there has been limited contribution to the understanding of Martian simulants responses under different loading scenarios, and this thesis intends to provide unique contributions in this area of research. The parameters obtained by this investigation can potentially serve to provide additional engineering knowledge required for future settlement activities and planetary surface exploration.

In addition, the mechanistic characterization of JSC Mars-1 can help to evaluate its feasibility to be used as a local construction material. This practice is called *in-situ* resource utilization (ISRU), which is one of the most important criteria in developing research associated with Martian settlement activities and planetary surface exploration. A full evaluation of the mechanical responses of JSC Mars-1 was conducted by considering a variety of preparation techniques based on the following parameters:

Table 1: Parameters influencing JSC Mars-1 Mechanical Properties.

External Parameters	Physical Parameters
Methods of densification	Impact of particle angularity index (<i>AI</i>)
Initial relative compaction (<i>RC%</i>) values	Impact of particle sphericity index (<i>SI</i>)
Confining pressure (σ_3)	Impact of particle chemical properties
Normal pressure (σ_N)	Particle texture
Strain Rate (<i>SR</i>)	Particle-size distribution

In order to simulate the mechanical performance of JSC Mars-1, the input parameters listed in Table 1 were used for laboratory analysis. The influence of these parameters in the mechanical

performance of JSC Mars-1 was studied by measuring the settlement and strength properties. These properties are listed in Table 2.

Table 2: Measured Mechanical and Settlement Properties for JSC Mars-1.

Settlement Properties	Strength Properties
Pre-compression pressure (σ'_p)	Particle toughness
Rebound Index (C_s)	Cohesion (c)
Coefficient of volume compressibility (M_v)	Angle of internal friction (ϕ°)
Compressibility Index (C_c)	Angle of dilation (ψ°)
-	Shear strength (τ)

Figure 1 provides an overview of the experiment matrix implemented by this investigation.

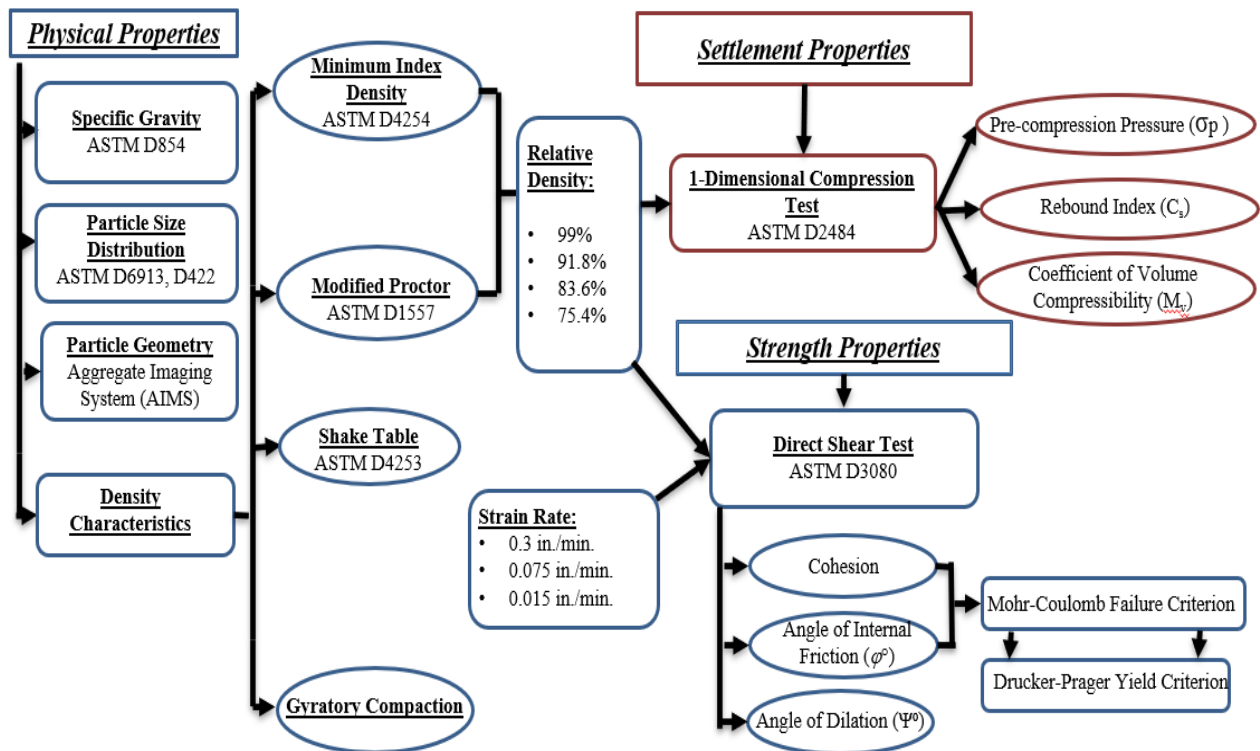


Figure 1. Laboratory Experiment Flow Chart

Table 3: Laboratory Experiment Matrix

Properties	Test Type		Output Parameter(s)	Number of Specimens	Amount of material (gr.)	
Physical and Textural Properties	<i>Specific Gravity</i> <i>ASTM D854</i>		G_s : Specific Gravity	4	240	
	<i>Particle Size Distribution</i> <i>(ASTM D6913, D422)</i>		C_u : Coefficient of Uniformity C_c : Coefficient of Curvature	8	800	
	<i>Particle Geometry-Aggregate Imaging System (AIMS)</i>		Angularity Index Sphericity Index	8	400	
	<i>Density Measurements</i>	<i>Modified Proctor</i> <i>(ASTM D1557)</i>		ρ_{max} : Maximum Dry Density	4	9,200
		<i>Vibration</i>	<i>Shake Table</i> <i>(ASTM D4253)</i>		20	36,000
			<i>Vibratory Hammer</i>		2	3,200
		<i>Gyratory Compaction</i>			24	36,000
<i>Minimum Index Density</i> <i>(ASTM D4254)</i>		ρ_{min} : Minimum Dry Density	8	12,800		
<i>Electrical Resistivity</i> <i>(Tex-129-E)</i>		R: Soil Resistivity @ 14 different moisture contents	28	1,500		
Mechanical Properties	<i>Particle Crushing</i> <i>(ASTM D422)</i>	<i>Different Compaction Methods</i>	ΔC_u : Coefficient of Uniformity ΔC_c : Coefficient of Curvature $\Delta p_{\#200}$: Concentration of material passing the #200 sieve	10	1,500	
	<i>Direct Shear Test</i> <i>(ASTM D3080)</i>		<i>4-Relative Compaction Levels</i>	ϕ : Angle of Internal Friction c : Cohesion Ψ : Angle of Dilation τ : Shear Strength	217	19,530
		<i>3-Strain Rates</i>				
<i>1-D Compression test</i> <i>(ASTM D2484)</i>	<i>3-Relative Compaction Levels</i>	σ_p : Pre-compression Pressure M_v : Coefficient of Volume Compressibility C_s : Rebound Index	12	1,080		
Total:				345	120,750	

As shown in Table 3, the amount of JSC Mars-1 material required to perform the tests included in the experiment matrix was of about 120,750 grams. The material was provided by the NASA Johnson Space Center. With the exception of the minimum index density, all of the tests are considered destructive. This is due to the alteration of the gradation parameters and the particle's size as a result of the static and dynamic loads applied over the simulant specimens. Therefore, undisturbed material was used for each of the tests performed.

1.2 Organization

The structure of this thesis is as follows:

Chapter 2 provides a brief description of the Martian geological and topographic conditions of the locations relevant to this thesis. These locations correspond to the landing and exploration sites where experimental data was collected by the Viking 1, Viking 2, and Pathfinder missions. This data that was used to develop regolith simulants like JSC Mars-1. This chapter also highlights the similarities in the regolith chemical composition at these three locations and that of JSC Mars-1. Chapter 2 also provides an overview of the naturally occurring densification processes expected on Mars.

Chapter 3 defines the standard procedures used for the measurement of the JSC Mars-1 index properties. These standards include particle-size distribution and Atterberg limits.

Chapter 4 investigates the experimental approach used for the determination of the JSC Mars-1 particle morphology properties. Two major particle morphology properties are presented in this chapter: particle angularity and sphericity. The influence of the angularity index in the mechanical performance of JSC Mars-1 is further studied in Chapter 8.

Chapter 5 investigates the variability of the JSC Mars-1 electrical resistivity values depending on its moisture content.

Chapter 6 studies the available densification procedures that can be performed in the laboratory. These procedures may represent different field scenarios and include the following: compaction by impact, vibration, and gyration. The chapter discusses how the compaction energy (*CE*) differs for each procedure, and its influence on the performance of JSC Mars-1 based on the final achieved density values and the particle crushing behavior. Compaction by impact, which is the densification procedure that resulted in the highest density, was selected as the soil preparation technique used for the test procedures described in Chapter 7. The term relative compaction (*RC%*) is introduced as one of the input parameters used in the laboratory modeling of the mechanical performance of JSC Mars-1.

Chapter 7 studies the variability of the mechanical properties of JSC Mars-1. This variability depends on four levels of relative compaction, six confining pressure levels (σ_3), and three load application rates. Major tests are presented in this chapter, including a 1-dimensional compressibility test and direct shear testing. The data obtained from the computed Mohr-Coulomb failure envelopes was rearranged in unique plots that analyze the impact that load and density conditions have on JSC Mars-1 in terms of cohesion (*c*), angle of internal friction (ϕ°), and angle of dilation (ψ°).

Chapter 8 introduces a Martian simulant prototype, EP-Limestone, with an identical particle-size distribution as JSC Mars-1. EP-Limestone differs from JSC Mars-1 in terms of particle morphology and chemical composition. The purpose of this chapter is to provide a side-by-side comparison of the mechanical properties of these two simulants.

Chapter 9 concludes this thesis with a summary of the results and their implications to Martian loading scenarios. Proposals for future work are also provided.

CHAPTER 2: LITERATURE REVIEW

2.1 Relating JSC Mars-1 with Martian Native Regolith Materials

It is essential to define the Martian surface regions that JSC Mars-1 represents. These locations are based on the landing sites where experimental data was obtained by the Viking1, Viking 2, and Pathfinder Missions. The main aspects used for these correlations are the similarities in terms of topographic and geological conditions of these locations. Furthermore, the likeness of the chemical composition of JSC Mars-1 with the native regolith at the Martian landing sites is also considered (Table 5).

2.1.1 MARTIAN SURFACE GEOLOGICAL UNITS AND PERIODS

As mentioned above, JSC Mars-1 was developed based on the experimental data obtained at the Viking 1, Viking 2, and Pathfinder landing sites. These sites can be delineated based on their enclosing geological units and periods. The identification of the Martian regions that can potentially be represented by JSC Mars-1 results important in determining the influence of the mechanical properties of future touchdown areas.

The geologic history of Mars is divided into three broad time periods. These are the Noachian, Hesperian, and Amazonian, which are subdivided into the Early Noachian, Middle Noachian, Late Noachian, Early Hesperian, Late Hesperian, Early Amazonian, Middle Amazonian, and Late Amazonian Epochs (Coles et al., 2019).

The Noachian Epochs were characterized by high rates of meteorite impacts, valley formation, weathering, and erosion. Subsequently, during the Hesperian Epochs, at least 30% of the Martian resurfacing continued as a consequence of relatively high rates of volcanism activity. Hesperian Epoch is also known as the main era of water flooding. Furthermore, during the Amazonian Epochs, volcanic activity and water flooding tended to be reduced, and the formation

of glacial deposits started to occur. In other words, Martian Epochs are defined by the number of meteorites impacts, volcanic activity, water history (Carr and Head III, 2010). A representation of the Martian geological activity as a function of time is provided in Figure 2.

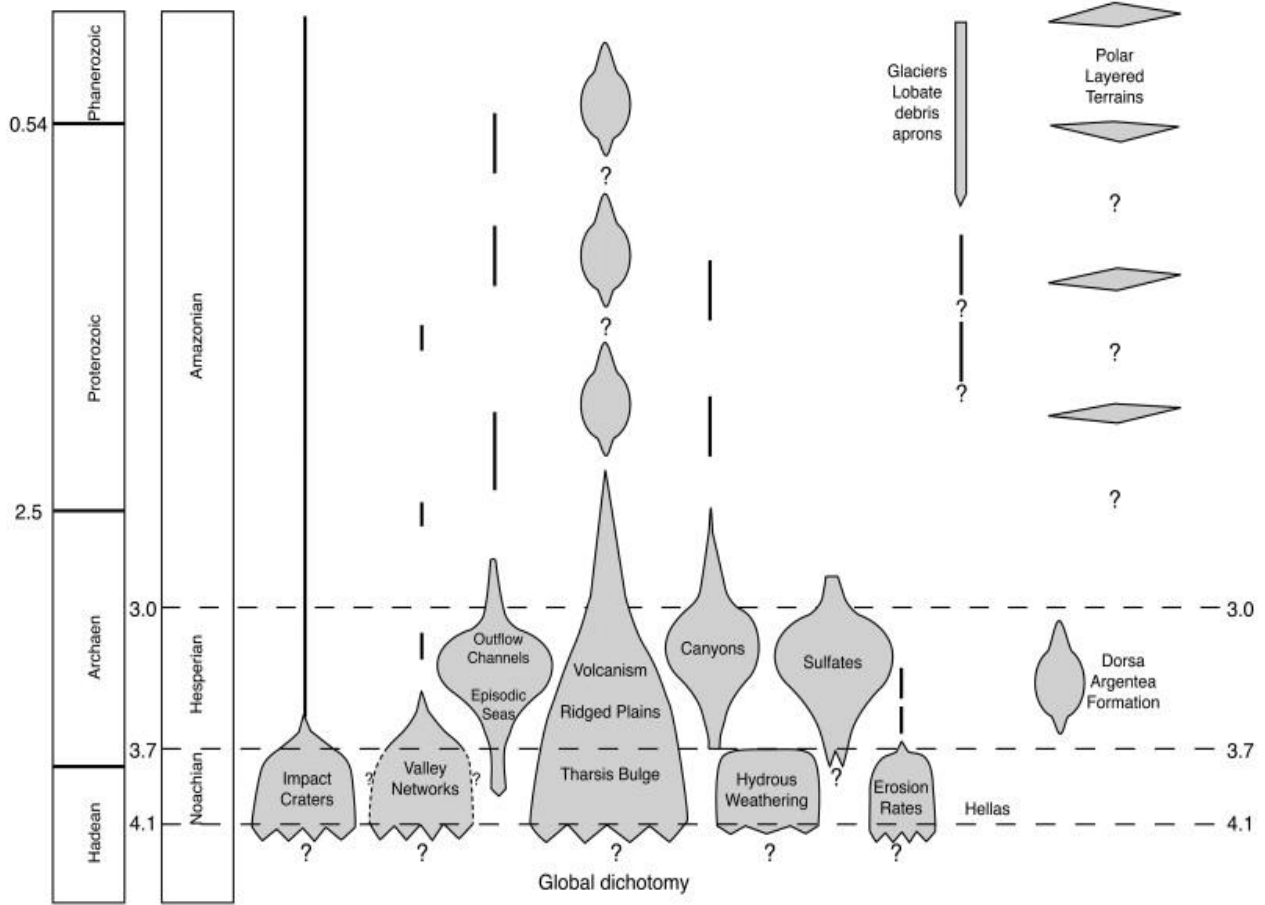


Figure 2. Geological Activity as a function of time on Mars (Carr and Head III, 2010). The approximate boundaries of Martian time periods are shown in giga years (Gyr.) (Hartman and Neukum, 2001). Terrestrial time periods are shown at the left-hand side (Head, 2006).

The geological period associated with the Viking 1, Pathfinder, and Viking 2 landing sites, is the Hesperian Period. At the same time, the geological units where the Viking 1 and Pathfinder landing sites are located, correspond with the Hesperian transition outflow channel (Hto). On the other hand, the Viking 2 landing site is located within the Late Hesperian lowland unit (IHI).

The similarities in the chemical composition of surface regolith at the various Mars landing sites (Table 5) are associated with the geologic systems and time periods of the red planet. The geologic map developed by Tanaka et al. (2014) (Figure 3), shows the locations of these landing sites with respect to the terranes of the Hesperian age.

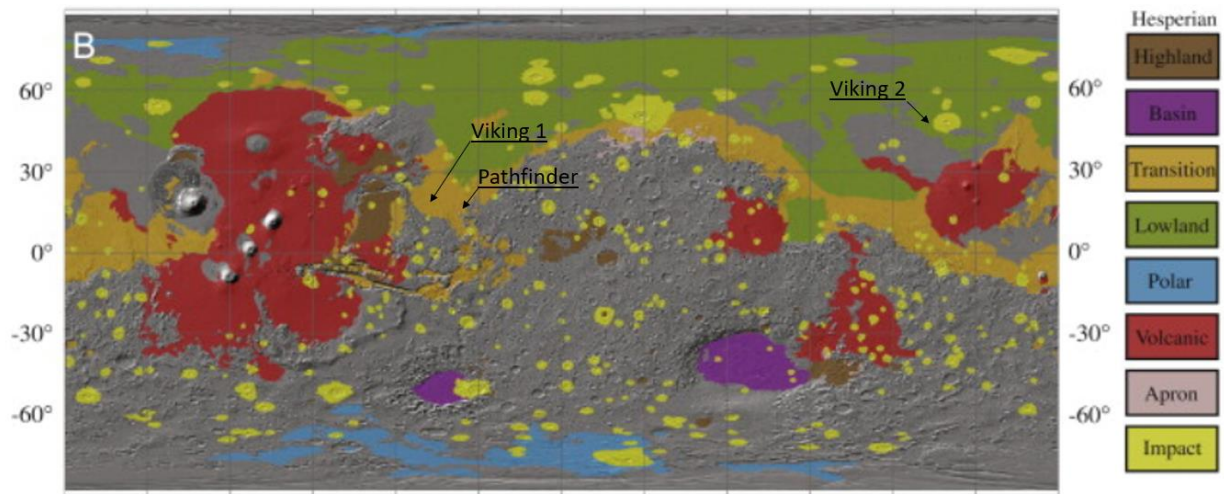


Figure 3. Hesperian Epochs with subject landing sites (Tanaka, et al., 2014)

As shown in Figure 3, the boundaries of the Hesperian geological unit are mainly located in the north hemisphere of the planet. This is due to the hemispheric dichotomy of the planet. The surface of Mars is characterized by several large-scale features. One of the most prominent features is the hemispheric dichotomy. This dichotomy is mainly associated with the difference in the elevation, in crater densities, and crust thicknesses between the northern lowlands and southern highlands (Smith et al., 2003). The formation of global dichotomy is considered the oldest geological event recorded (Carr, 2006). This formation may have set the stage for the growth of the Tharsis volcanic and tectonic provinces and most of the subsequent geologic evolution of Mars. In fact, the giant volcanoes and vast canyons of the Tharsis volcanic and tectonic province are dominate the Martian landscape (Watters et al., 2007). As mentioned before, the volcanic activity during the Hesperian Epochs constitutes about the 30% of the Martian resurfacing.

To conclude, the landing sites where the Viking 1, Viking 2, and Pathfinder Missions touched down, are strongly correlated in terms of geological aspects. These sites are all located within the lowland northern region, and in the Hesperian geological unit. The similarities in terms of topography are explained in Section 2.1.2.

2.1.2 MARTIAN TOPOGRAPHY

Topographic conditions are also similar for the Viking 1, Viking 2, and Pathfinder landing sites. Table 4 provides an overview of the primarily topographic aspects of the geological units associated with these locations (Tanaka et al., 2014).

Table 4: Mean Elevation and slope statistics for Mars geological units associated with Viking 1, Viking 2, and Pathfinder landing sites.

Geological Unit	Corresponding Landing Site(s)	Area (10⁶ km²)	Mean Elevation (m)	Mean Slope (deg)
Hesperian transition outflow channel (Hto)	Viking 1 Pathfinder	1.35	-3,214	0.98
Late Hesperian lowland unit (IHI)	Viking 2	17.28	-4,347	0.42

The topographic conditions associated with the subject landing sites, and their corresponding geological units, are of primary interest of this thesis. As discussed in Sections 2.1.1 and 2.2, JSC Mars-1 was developed with experimental data obtained at these landing sites. Therefore, it is important to provide an approach of the topographic and geological regions in which these native regolith materials may extend.

Furthermore, the mean slope measured at the Hesperian geological units that are associated with the subject landing sites may provide an indication of the in-situ performance of the mechanical properties of these regolith materials. The main mechanical properties associated with

slope stability are the angle of repose, or angle of internal friction (ϕ^0), and cohesion (c). For the purposes of this thesis, these properties are mechanistically characterized under a variety of simulated conditions in Chapter 7.

As shown in Figure 4, these locations are approximately located at similar elevations.

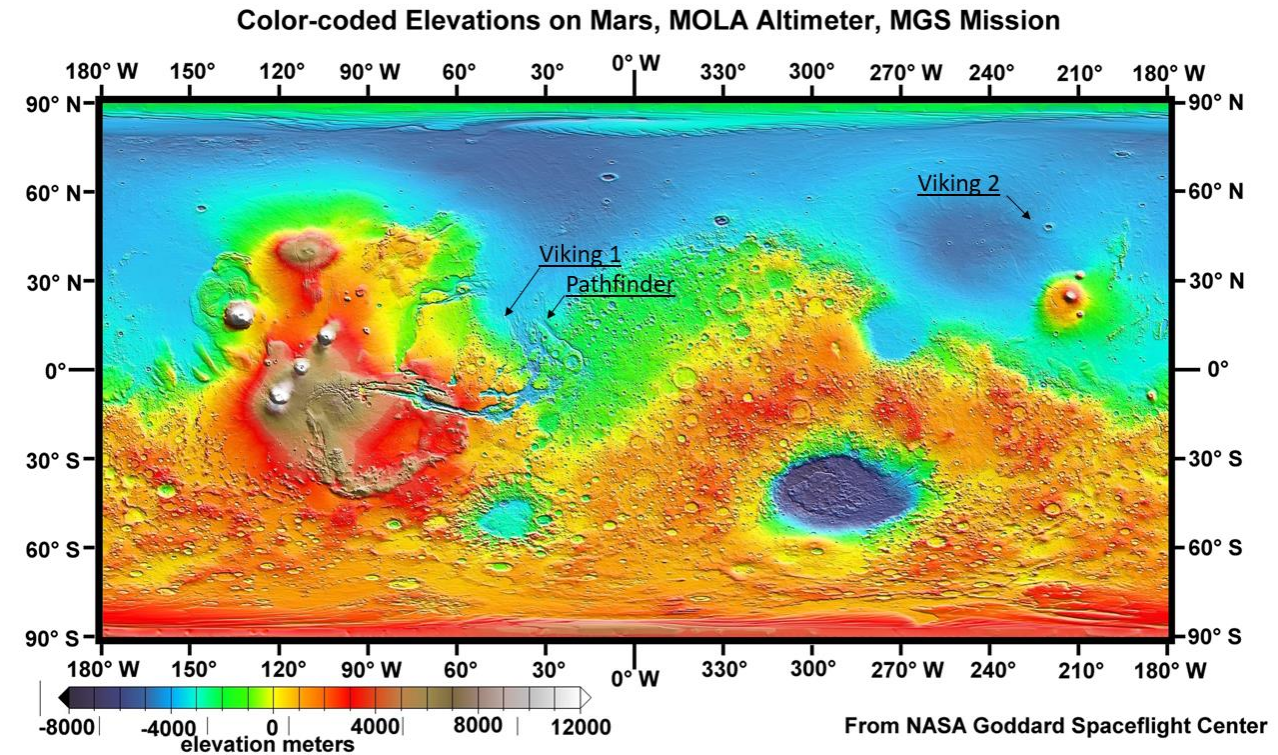


Figure 4. Global Topographic Map of Mars. Color coded by elevation as determined by the Mars Orbital Laser Altimeter (MOLA).

The present section, along with Section 2.1.1. have shown how the native regolith materials associated with the Viking 1, Viking 2, and Pathfinder Missions are similar with one another in terms of geological and topographical aspects. Section 2.2 provides an overview of the development of the regolith simulant JSC Mars-1, and how this material simulant is related with the afore mentioned native regolith materials.

2.2 Development of JSC Mars-1 Regolith Simulant

Mars is a terrestrial planet, which means that it has a core made of metallic iron and nickel encased in a less dense silicate mantle and crust (Nimmo and Tanaka, 2005).

Data shows the primary chemical elements on Mars's crust are silicon, oxygen, iron, magnesium, aluminum, calcium, and potassium (Allen et al., 2004). As shown in Table 5, these chemical elements are main constituents of both native regolith studied at the Viking 1, Viking 2, and Pathfinder landing sites, and JSC Mars-1.

The data gathered by Viking 1, Viking 2, and Pathfinder landers enabled the determination of regolith chemical compositions, particle-size distributions, and particle porosity at each landing site (Allen et al., 2004). Based on these assessments, NASA was able to develop the JSC Mars-1 simulant (Allen et al., 2004). JSC Mars-1 was developed using weathered volcanic ash, sourced from the Pu'u Nene cinder cone on the island of Hawaii, and characterized at the NASA Johnson Space Center (JSC). JSC Mars-1 is a mixture of ash particles with alteration rinds of various thicknesses (Allen et al., 2004). The ash is composed of finely crystalline and glassy particles of Hawaiite composition (Allen et al., 2004).

Comparisons of the JSC Mars-1 simulant composition to the regolith at the Viking 1 and 2, and Pathfinder landing sites were conducted by Allen et al. (2004). As shown in Table 5, the chemical compositions of the regolith materials studied at Viking 1, Viking 2, and Pathfinder landing sites are almost identical. As discussed in Sections 2.1.1 and 2.1.2, the geological and topographical conditions are similar at the three landing sites. Another explanation to the similarity in the chemical composition of the regolith materials encountered at these landing sites is that the chemical constituents of these materials are volatile. In fact, data suggested that the Mars regolith has a chemical component that is distributed planet-wide, probably by the wind (Allen et al., 2004).

Table 5 shows the chemical composition of JSC Mars-1 compared to native regolith materials encountered at the three landing sites.

Table 5. Chemical Compositions of Martian Regolith Materials and JSC Mars-1¹

Oxide	Landing Sites			JSC-Mars 1	
	Viking 1	Viking 2	Pathfinder		
	Wt. (%) *	Wt. (%) *	Wt. (%) **	Wt. (%) ***	Wt. (%) ****
SiO₂	43	43	44	34.5	43.5
Al₂O₃	7.3	7.0	7.5	18.5	23.3
TiO₂	0.66	0.56	1.1	3.0	3.8
Fe₂O₃	18.5	17.8	16.5	12.4	15.6
MnO	N.A.	N.A.	N.A.	0.2	0.3
CaO	5.9	5.7	5.6	4.9	6.2
MgO	6.0	6.0	7.0	2.7	3.4
K₂O	<0.15	<0.15	0.3	0.5	0.6
Na₂O	N.A.	N.A.	2.1	1.9	2.4
P₂O₅	N.A.	N.A.	N.A.	0.7	0.9
SO₃	6.6	8.1	4.9	N.A.	N.A.
Cl	0.7	0.5	0.5	N.A.	N.A.

* Viking landers 1 and 2 XRF (mean of 3)

** Pathfinder APXS (mean of 5, normalized to 44 wt. % SiO₂)

*** XRF

**** XRF (volatile-free, normalized)

Similarities between JSC Mars-1 and the native regolith materials encountered at Viking 1, Viking 2, and Pathfinder landing sites make this simulant suitable for characterizing the

¹ (Allen et al., 2004)

geotechnical properties and predicting the performance of these regolith materials. These similarities include particle size distribution, mineralogy, and chemical composition (Allen et al., 2004).

However, experimental results from a single regolith simulant cannot be expected to completely characterize the complete physical and mechanical properties of the Martian surface (Scott et al., 2017). Therefore, in the effort to delineate the Martian regions that can be represented by JSC Mars-1, the locations corresponding with the Viking 1, Viking 2, and Pathfinder landing sites have been studied in terms of geological and topographic conditions. In addition, as a consequence of winds, the regolith is relatively homogenous across Mars (Allen et al., 2004).

The mechanical properties of Martian regolith affect geomorphological processes like mass wasting, crater formation, and erosion, which are important factors in understanding the evolution of the Martian surface (Perko et al., 2001). For example, particle size distribution is a key component for understanding the mechanical properties of the Martian regolith. It affects the soil strength and compressibility, along with its optical, thermal, and seismic properties (Perko et al., 2001). Data collected from Viking, Pathfinder, and the Mars Exploration Rover (MER) Mission were analyzed to determine that most of the surface regolith on Mars consists of particles $< 50 \mu\text{m}$ in size (Zimmerman, 2016). Images from MER were used to determine that the particle size of fine-grained dust on Mars ranges up to $45 \mu\text{m}$ while fewer fine sands had a particle size of approximately $130\text{-}160 \mu\text{m}$ (Zimmerman, 2016). Without returned samples of soil from Mars, understanding of the regolith mechanical and physical properties must rely on simulants.

2.3 Loading Conditions and Densification Processes of Martian Regolith

Soils are stress-dependent materials in that soil strength is associated with external loading, drainage conditions, relative compaction, and rate of deformation (Prevost and Popescu, 1996). For this investigation, drainage conditions are not considered, given that hygroscopic moisture has not yet been discovered on Mars. Therefore, the parameters that are considered in this thesis, with respect to the performance of the mechanical properties of JSC Mars-1, are initial relative compaction ($RC\%$) and loading conditions (magnitude and rate of load application).

This thesis explores different methods of compaction that result in variable rearrangement of JSC Mars-1 particles. In the field, densification processes of regolith can be produced due to meteorite impacts, seismic activity, and anthropogenic effects (e.g., rover traverses, footprints, etc.). For example, compaction by vibration will result in a different regolith particle arrangement than compaction by impact or appliance of a quasi-static load (Massarsch, 2002). The shake table method, which is a laboratory method used to replicate compaction by vibration in the field, results in a better simulation of field densification processes compared to compaction by impact. The comparison of these compaction methods are discussed in Chapter 6.

As a result, the best compaction technique for a given regolith material depends entirely on its particle-size distribution (Broms and Lars Forssblad, 1968). The purpose of exploring different compaction techniques is to determine the influence that the resulting density has on the mechanical properties of JSC Mars-1.

The variability of the levels of confining pressure (σ_3) exerted on regolith simulants in the laboratory is useful for representing external loading conditions present in the Martian surface. Willman et al. (1995) performed a series of consolidated, drained, triaxial tests using three levels

of confinement. They correlated the measured mechanical properties with in-situ overburden pressures (σ_1) at different depths below the lunar surface by using the equation:

$$\sigma_1 = g \cdot \rho \cdot z \quad (1),$$

where

σ_1 is overburden pressure, in kN m^{-2} ; g is gravitational acceleration, in m s^{-2} ; ρ is bulk density, in kg m^{-3} ; and z is depth, in m.

CHAPTER 3: INDEX PROPERTIES OF JSC MARS-1

3.1 Particle Size Distribution

Particle-size distribution parameters define the performance of the mechanical properties of regolith materials (Carrier et al., 1973). Therefore, the characterization of these parameters is fundamental in the study of JSC Mars-1 (Morgan et al., 2018). The particle-size distribution curve, which is defined as the relationship of the relative concentration of particles present according to size. For geomaterials, the particle's size is classified in two main groups: coarse- and fine-grained particles.

Coarse-grained particles are classified as either well-graded or poorly-graded. For engineering design purposes, the suitability of a given coarse-grained soil to be used in a certain type of geo-structure is mainly determined by this parameter. For example, well-graded soils can provide satisfactory bearing capacity for foundations, while poorly-graded soils are adequate for drainage purposes due to their high hydraulic conductivity. To determine if coarse-grained soils are either well- or poorly-graded, it is necessary to compute the coefficient of curvature (C_c) and coefficient of uniformity (C_u) using the following equation (ASTM C136):

$$C_c = \frac{D_{60}}{D_{30}} \quad C_u = \frac{D_{30}^2}{D_{10}D_{60}} \quad (2)$$

Where:

D_{10} : Effective size, diameter of the mesh size at which 10% of the total sample is passing.

D_{30} : Diameter of the mesh size at which 30% of the total sample is passing.

D_{60} : Diameter of the mesh size at which 60% of the total sample is passing.

As shown in Figure 5 a particle-size distribution curve of JSC Mars-1 was developed on this study. The coarse portion was characterized by performing a mechanical sieve analysis

(ASTM C136 and C117). Subsequently, the gradation parameters corresponding with the fine portion of the material were determined by following the hydrometer sieve analysis test standard (ASTM D422) and Atterberg limits test (ASTM D4318).

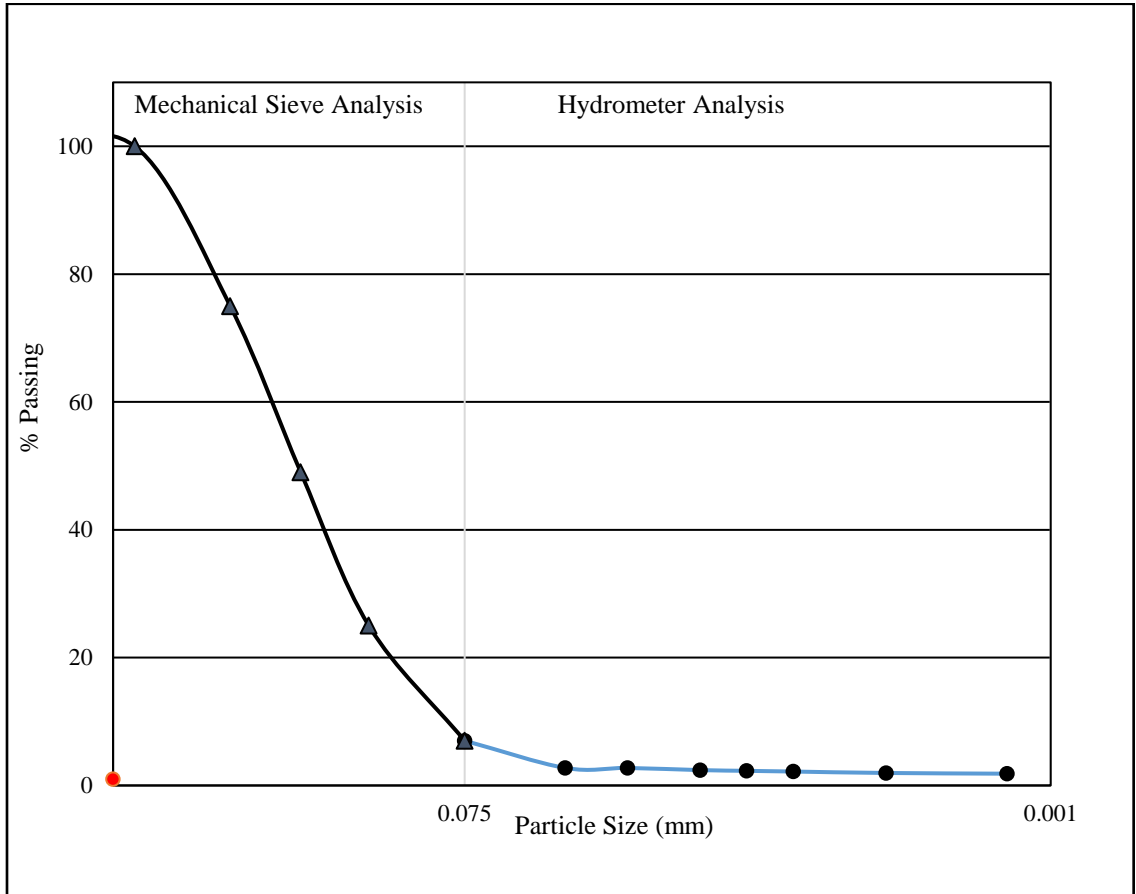


Figure 5. Particle Size Distribution Curve of JSC Mars-1.

For JSC Mars-1, the C_C and C_U values were determined to be 1.23 and 4.31, respectively. Based on these values, and the grain size distribution curve (Figure 5), the material is classified as poorly graded sand with silt (SP-SM), according to the Unified Soil Classification System (USCS; ASTM D2487).

3.2 Characterization of the Fine-grained Particles of JSC Mars-1

In contrast with coarse-grained particles, fine-grained particles are characterized by their moisture absorption capacity and particle size. Fine-grained particles tend to adsorb water molecules, and consequently, they increase their volume when wet. The result is instability in terms of load-bearing capacity.

In the engineering industry, the moisture absorption capacity of geomaterials is characterized with the Atterberg limits test (ASTM D4318). These limits were firstly defined by Albert Atterberg, in 1911. The by Atterberg limits are used to define the behavior of fine-grained soils at different moisture contents. Later on, Albert Casagrande (1932) refined these limits and standardized the tests used to characterize the soil states: solid, semi-solid, plastic, and liquid. For example, fine-grained soils are considered to be in the solid state if its moisture content is below its shrinkage limit (Casagrande, 1932). When the moisture content is below the shrinkage limit, its volume change potential is negligible (Casagrande, 1932). The semi-solid state is achieved if the soil has a moisture content between the shrinkage limit and the plastic limit (Casagrande, 1932). As the moisture content present in fine-grained soils increases, the volume of the soil tends to increase. This causes a separation between particles, which results a decrease in shear strength (Casagrande, 1932). Fine-grained soils with a moisture content that ranges between the plastic and liquid limits are considered to be in a plastic state (Casagrande, 1932). The range between the plastic and the liquid limit is known as the plasticity index (PI ; Casagrande, 1932). PI is used as an indication of soil moisture susceptibility. The higher the PI , the higher will be the soil potential volume change index (PVI). Finally, fine-grained soils with moisture content higher than the liquid limit is considered to be in a liquid state and cannot sustain shear stress (Casagrande, 1932).

The liquid limit of JSC Mars-1 was tried to be characterized by following ASTM D4318. This test consists of counting the number of blows required to close the groove of a given geomaterial in the Casagrande cup (Figure 7) at 1-inch. The moisture content at which the groove closes after 25 blows, is defined as the liquid limit.

The output parameters obtained from the Atterberg limits test, particularly liquid limit and plasticity index, are plotted on the Casagrande Plasticity Chart (Casagrande, 1932; Figure 6) which is used to distinguish between clayey and silty soils.

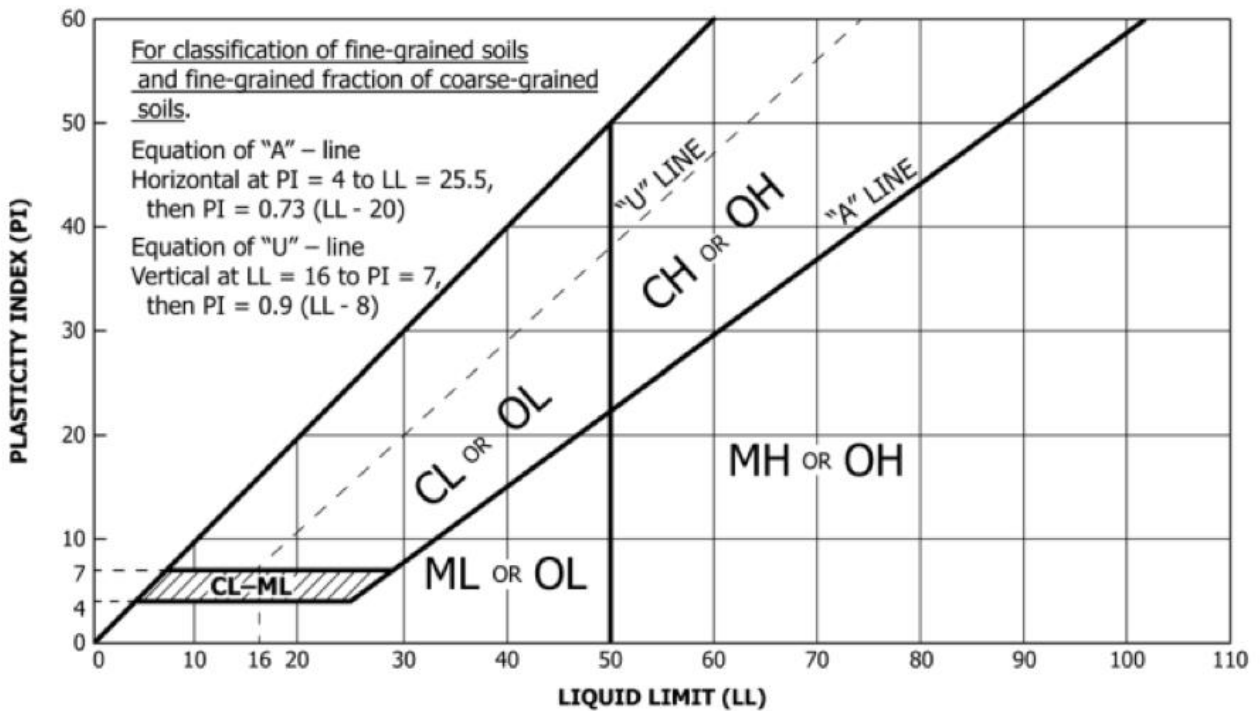


Figure 6: Casagrande Plasticity Chart.

The liquid limit of JSC Mars-1 was tried to be measured at different moisture contents. The experiment was repeated twice to obtain accurate test results. As shown in Figure 7, the absence of adhesional forces between JSC Mars-1 and the Casagrande cup resulted in the failure to perform

this test at any moisture content. This is an indication of the low moisture susceptibility exhibited by JSC Mars-1.



Figure 7. Failure to perform the liquid limit test in the Casagrande device due to absence of adhesion forces between the soil particles and the Casagrande cup.

A failure to perform the liquid limit test, at any moisture content, represent the low, or negligible plasticity that JSC Mars-1 has. The characterization of the fine-grained portion of geomaterials can be achieved by the Atterberg limits, provided that they are moisture susceptible enough to produce values (Liquid limit and plasticity index) to be plotted in the Casagrande Plasticity Chart.

Given that the characterization of the fine-grained portion of JSC Mars-1 was not possible by using the Atterberg limits test, a hydrometer test was performed to compute the particle-size distribution of the fine portion of JSC Mars-1.

The hydrometer test is used to measure the relative density of liquids based on Stoke's Law (ASTM D422). To perform the test, soil particles, assumed to have a spherical shape, are temporarily suspended in distilled water. The particles will settle in water by falling at a certain

settling velocity associated with the particle's diameter. The settling velocity (v) is determined using the equation:

$$v = \frac{2(\rho_p - \rho_f)}{9\mu} gR^2 \quad (3),$$

where ρ_p is the density of the particles (kg m^{-3}); ρ_f is the density of the fluid (kg m^{-3}); μ is the dynamic viscosity ($\text{kg m}^{-1} \text{s}^{-1}$); g is the gravitational acceleration (m s^{-2}); and R is particle diameter (m).

To compute the particle-size distribution of the fine portion of JSC Mars-1. A hydrometer type 151H and a 1-liter sedimentation flask was used by following standard procedure ASTM D422. The JSC Mars-1 particle's diameter was measured at different sedimentation times. The experiment was repeated twice to obtain accurate test results.

Hydrometer analysis, in combination with mechanical sieve analysis, revealed that the majority of fine particles in JSC Mars-1 are silt-sized (72.9% silt and 27.1% clay). This reaffirms the outcome of the Atterberg limits test. Table 6 provides a summary of the results obtained from the mechanical and hydrometer sieve analysis analysis.

Table 6. JSC Mars-1 Composition by Soil Group

Soil Group	Concentration (%)
Gravel (G)	0
Sand (S)	93
Silt (M)	5.1
Clay (C)	1.9

CHAPTER 4: PARTICLE MORPHOLOGY

4.1 Particle Angularity

The spherical and angular characteristics of the coarse portion of JSC Mars-1 were analyzed using a state-of-the-art Aggregate Image System (AIMS). This system captures the pattern spectrum of each particle and normalizes the calculated angular and shape ratios in angularity and sphericity indices. Lees (1964) defines the angularity index as the ratio of the bounding edge angles and the distance of the edges from the center of the particle. On the other hand, sphericity is defined as the ratio of the surface area of a sphere of the same volume as the particle to the actual surface area of the particle (Wadell, 1933).

The contribution that particle angularity and sphericity has to the performance of geomaterials is significant. The inter-locking effect of particles is associated with high angularity index values, which results in a higher angle of repose and dilatancy behavior (Stark et al., 2014).



Figure 8. JSC Mars-1 Particles in the AIMS chamber.

To determine angularity index with the AIMS, we apply the radius method developed by Masad et al. (2000). Basically, the aggregate imaging system records the records the particles' radii in all directions and that of an equivalent ellipse (Masad et al., 2004). For example, a perfectly shaped circle would have an angularity index of zero (Wang et al., 2018). The angularity index is expressed as follows:

$$AI = \sum_{\theta=0}^{355} \frac{|R_{\theta} - R_{EE\theta}|}{R_{EE\theta}} \quad (4),$$

where R_{θ} is the radius of the particle at a given angle and $R_{EE\theta}$ is the radius of the equivalent circumscribed ellipse.

The angularity index obtained with Equation (4) is expressed according to the Krumbein scale, with values that range from 0 to 10,000 (Krumbein, 1941, Stanley and So, 2006, Wadell, 1933). The majority of the coarse particles in JSC Mars-1 are classified as moderately (2,100-3,975) to highly (3,975-5,400) angular on the Krumbein scale.

AIMS revealed that the angularity index increase with the diameter of the particles (Figure 9). In other words, the larger the grains, the higher is the number of fractured faces. This phenomenon is associated with the crushing behavior that this material exhibits (see Chapter 6). As discussed in Section 6.4, JSC Mars-1 coarse-grained particles are more susceptible to degradation than fined-grained particles. In fact, particle breakage, which is defined as the generation of fines, tends to increase with particle size, given that larger particles contain more surface area to be crushed, in higher probability (Hardin, 1985). The relationship of the angularity index with particle-size is represented in Figure 9.

Particle assemblies that consist of flat and elongated shapes are more anisotropic in nature. The directional dependency of material properties in such assemblies is often detrimental to the

system's stability in dynamic loading conditions. For instance, dunes on Mars could be destabilized by vibrations induced by a nearby rover (Perko et al., 2006).

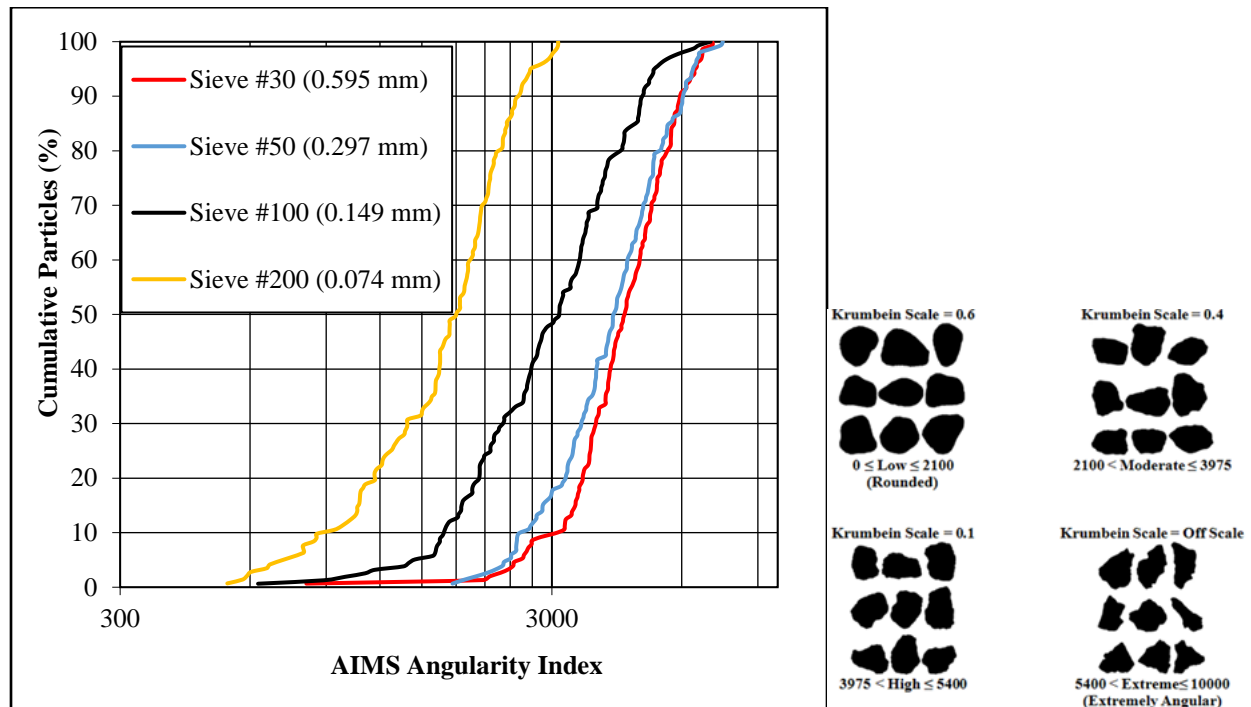


Figure 9. Characterization of angularity index for JSC-1 Mars using AIMS. (Left) Relationship of AIMS angularity index of individual particles grouped by four sieve standard sizes. (Right) Visual explanation of the Krumbein scale (Krumbein, 1941).

As shown in Figure 9, particle angularity is greatly influenced by particle size, with particles larger than 0.149 mm exhibiting higher angularity compared to particles smaller than 0.149 mm. Based on Krumbein angularity index analyses on over 200 particles, approximately 67% of particles in JSC Mars-1 larger than 0.149 mm in diameter exhibited high and extreme angularity indices (Table 7). High angularity indices range between 3,975 and 5,400 in the Krumbein scale. Whereas, extreme angularity indices range between 5,400 and 10,000. In other words, the concentration of JSC Mars-1 particles with low angularity ranges increases as particle diameter decreases, and the concentration of particles with high and extreme angularity index tends

to increase as particle diameter increases. The concentration of angular particles at low, moderate, high, and extreme ranges with respect to particle's size for JSC Mars-1 is represented in Table 7.

Table 7. Particle Size Concentration for a Range of Angularities.

Angularity Ranges	0.60mm, #30	0.30 mm, #50	0.15 mm, #100	0.075 mm, #200
	Particle Concentration (%)	Particle Concentration (%)	Particle Concentration (%)	Particle Concentration (%)
Low (0 – 2,100)	1.3	2.0	24.2	62.9
Moderate (2,100 – 3,975)	31.6	39.7	50.3	32.2
High (3,975 – 5,400)	45.4	39.1	21.7	3.5
Extreme (5,400 – 10,000)	21.7	19.2	3.8	1.4

4.2 Particle Sphericity

Sphericity is a relative indication of how round a particle is compared to a perfect sphere. High values of the sphericity index indicate elongated particles with an ellipsoidal shape. Low values of the sphericity index indicate circular shapes. The aspect ratio of a particle increases as the sphericity index is larger (Kong et al., 2019). AIMS can be used to determine sphericity using the equation:

$$S = \sqrt[3]{\frac{d_s d_l}{d_L^2}} \quad (5),$$

where d_s is the particle shortest diameter; d_l is the particle intermediate diameter; and d_L is the particle largest diameter.

Unlike the angularity index, the sphericity index does not vary significantly as a function of grain diameter for JSC Mars-1. This is due to the particle's crushing behavior exhibited by JSC Mars-1. As discussed in Chapter 1, the gradation of JSC Mars-1 is classified as poorly graded. In other words, the particle's sphericity does not vary significantly from one another in terms of group sizes. This leads to the principle that poorly graded particles are more susceptible to particle breakage due to the non-uniform distribution of stresses (Lee and Farhoomand, 1967). Most of the coarse particles in JSC Mars-1 exhibit a high degree of sphericity for all grain sizes (Figure 10; Table 8).

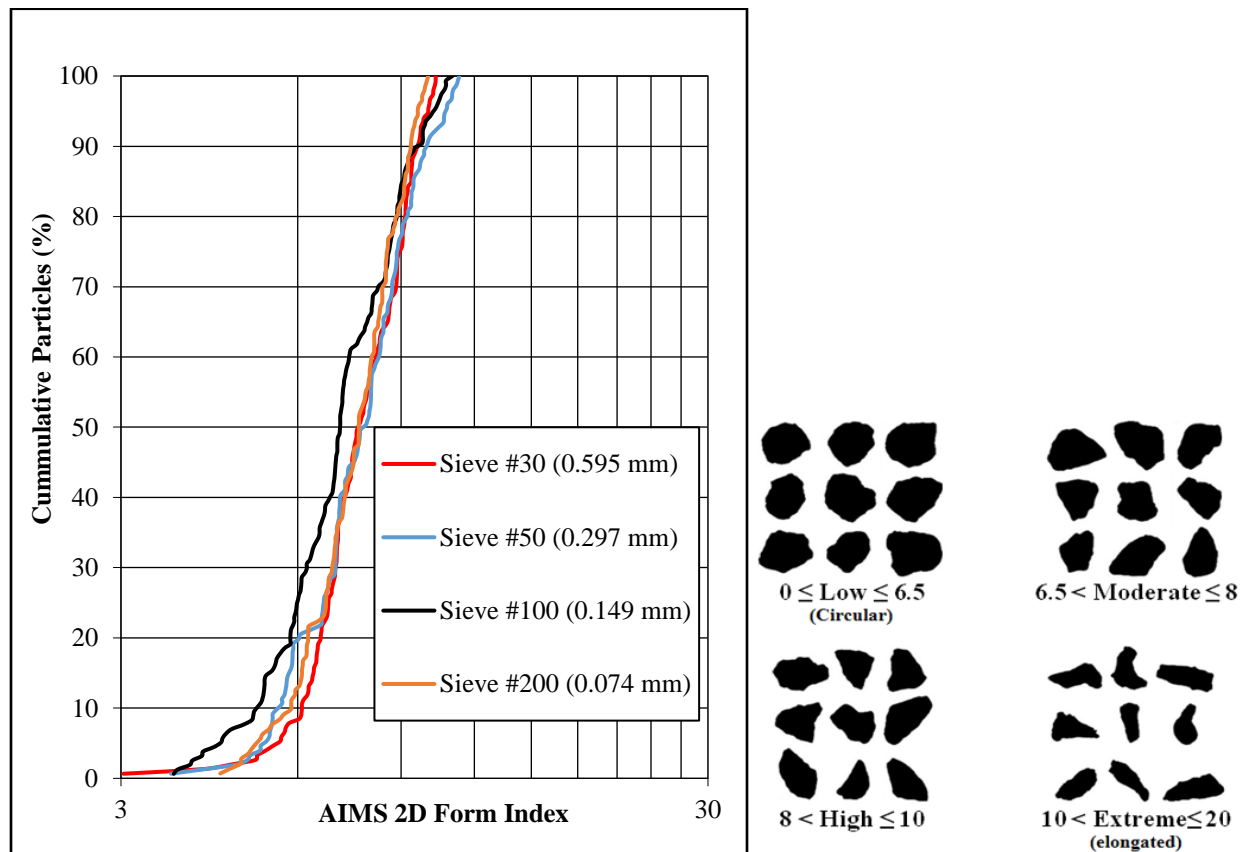


Figure 10. Particle sphericity distribution. (Left) Relationship of AIMS sphericity index of individual particles grouped by four sieve standard sizes. (Right) Visual explanation of the Krumbein scale (Krumbein, 1941).

Table 8. Particle Size Concentration for a Range of Sphericity Values.

Sphericity Ranges	0.60mm, #30	0.30 mm, #50	0.15 mm, #100	0.075 mm, #200
	Particle Concentration (%)	Particle Concentration (%)	Particle Concentration (%)	Particle Concentration (%)
Low (0 – 6.5)	18.4	19.2	30.6	21.0
Moderate (6.5 – 8)	34.9	29.1	29.3	30.8
High (8 – 10)	40.1	36.4	31.8	40.6
Extreme (10 – 20)	6.6	15.2	8.3	7.7

CHAPTER 5: ELECTRICAL RESISTIVITY

Electrical resistivity is defined as the ability of a material to resist electric current. In the construction industry, the electrical resistivity of soils is used to indicate the level of corrosiveness (Romanoff, 1989). A correlation between soil corrosivity and electrical resistivity for ferrous materials is shown in Table 9.

Table 9. Correlation Between Soil Corrosivity and Electrical Resistivity.²

Soil Resistivity in ohm-centimeters	Corrosivity Category
Greater than 10,000	Mildly Corrosive
2,001 to 10,000	Moderately Corrosive
1,001 to 2,000	Corrosive
0 to 1,000	Severely Corrosive

Given that soils are considered non-uniform materials, several factors affect the degree of electrical resistivity, even for the same soil type. Chemical composition and physical properties such as the presence of organic matter, particle-size distribution, and particle shape are some of the parameters that affect soil resistivity. Degree of saturation and degree of compaction are the most important factors that influence electrical resistivity values for a given soil type. The reason for this is the influence that air voids in the internal soil structure have on the degree of saturation and relative compaction. As relative compaction increases, the presence of air voids is reduced, and, therefore, the electrical resistivity is reduced. Similarly, the degree of saturation influences the electrical resistivity behavior of geomaterials as air voids are filled with water resulting in an increase in electrical conductivity (Han Kim et al., 2011).

² (Romanoff, 1989)

To determine the corrosivity category of JSC Mars-1, we characterize the relationship between electrical resistivity and moisture content at a single degree of relative compaction. We use a Miller box and the Vibroground Model 293 was implemented by using TxDOT standard TEX-129-E (TxDOT, 2017). The electrical resistivity of JSC Mars-1 was measured for different moisture contents. The experiment began with a moisture content of 0% and distilled water was added in increments of 50 ml. It is important to highlight that the specimens were prepared at a relative compaction value of 99.0%. The experiment was repeated twice to obtain accurate test results.

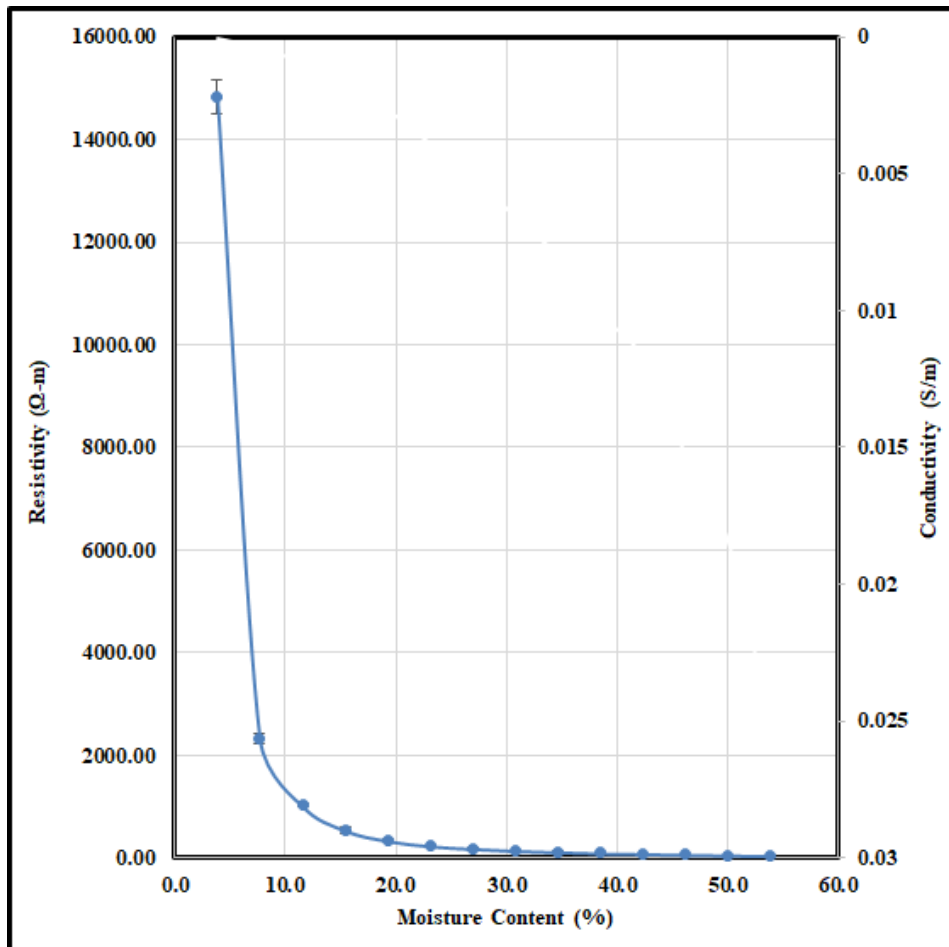


Figure 11. Electrical resistivity vs. moisture content for JSC Mars-1.

Table 10: Electrical Resistivity vs. Moisture Content for JSC Mars-1

Test No.	Resistivity (Ω-m)	Conductivity (S/m)	Standard Deviation	Moisture content (%)
1	15167.0	6.6E-05	329.7	3.8
2	2440.05	4.1E-04	98.9	7.7
3	1055.16	9.5E-04	33.0	11.5
4	600.12	1.7E-03	59.4	15.4
5	375.90	2.7E-03	39.6	19.2
6	257.19	3.9E-03	23.1	23.1
7	204.44	4.9E-03	23.1	26.9
8	151.68	6.6E-03	9.9	30.8
9	125.30	8.0E-03	9.9	34.6
10	98.92	1.0E-02	6.6	38.5
11	85.73	1.2E-02	6.6	42.3
12	65.95	1.5E-02	0.7	46.2
13	54.74	1.8E-02	2.0	50.0
14	40.23	2.5E-02	0.7	53.8

As shown in Figure 11, the electrical resistivity value of JSC Mars-1 asymptotically approaches 0 Ω m for moisture contents in excess of 30%. This behavior indicates that the degree of saturation (S%) approaches 100% for moisture contents above 30%. In Figure 12, JSC Mars-1 was prepared with a moisture content of 34.6%, and water started to seep out of the compacted specimen, indicating that it had reached 100% saturation.



Figure 12. JSC Mars-1 in the Miller Box prepared at a relative compaction (RC%) of 99% and a moisture content of 34.6%. Note the seepage of water from the specimen, indicating the degree of saturation is 100%.

CHAPTER 6: DENSITY AND COMPACTION

The mechanical performance of geomaterials is strongly associated with relative density ($D_r\%$; Terzaghi, 1925). Relative density can be calculated as follows:

$$D_r \% = \frac{\rho_{dmax}(\rho_d - \rho_{dmin})}{\rho_d(\rho_{dmax} - \rho_{dmin})} \times 100 \quad (6),$$

where ρ_{dmax} is the maximum index density; ρ_{dmin} is the minimum index density; and ρ_d is the dry density at a given void ratio.

In other words, relative density is a function of the actual dry density with respect to the maximum and minimum achievable dry densities. On the other hand, relative compaction (RC%) is defined as the ratio of the actual dry density and maximum achievable density. To provide a comparison of the actual dry densities of JSC Mars-1 with respect to the maximum achievable density discussed in Section 6.4, relative compaction is used instead of relative density.

The variability of the mechanical properties such as strength, stiffness, moisture susceptibility, and settlement potential is strongly dependent on the degree of relative compaction (Dhir et al., 2018). There are several techniques to improve the mechanical properties of soil, with mechanical compaction being the most common one (Rogers et al., 1993). Several laboratory methods, to include compaction by impact, gyration, and vibration, have been developed to replicate the densification characteristics present in the field (Virgil Ping et al., 2002).

To measure the maximum dry density of JSC Mars-1, several compaction methods were used: impact, vibration, and gyration. One of the main parameters that can be used to compare these methods of compaction is the compaction energy (CE). Compaction energy, among maximum achievable density, and particle breakage, are used as a point of comparison in Section

6.4. Compaction energy is the result of a combination of different factors that are explained in the following sections, and is defined as the effort used in densification processes.

6.1 Minimum Index Density

The minimum index density was determined by following the ASTM D4254 test procedure, a method commonly known as the raining technique. As shown in Figure 13, the raining technique consists of pouring the oven-dried soil sample into a mold with a calibrated volume. The fall height and the pouring rate are controlled with a standardized funnel. The resulting amount of material contained in the unit volume is considered the lowest achievable density. The relationship between the minimum and maximum index density test results for JSC Mars-1 are shown on Figure 15.



Figure 13. JSC Mars-1 being poured in a calibrated mold by the raining technique.

6.2 Impact Compaction: Modified Effort

One of the most common testing methods used in industry to determine the maximum dry density is the modified Proctor test (ASTM D1557). This method consists of developing a moisture-density relationship that provides an indication of the amount of moisture required to reach a maximum dry density. In the densification process by using the modified Proctor test,

moisture acts a lubricant between the particles, and facilitates their rearrangement caused by impact. This rearrangement reduces the void ratio and therefore, produces an increase in the wet density. The achieved dry density is then measured by subtracting the amount of moisture required to achieve the given wet density. To develop the moisture-density relationship, the test is performed at several moisture contents. The amount of water required to achieve the maximum dry density is known as the optimum moisture content. However, since no hygroscopic moisture has yet been found on Mars, and to replicate the densification processes by impact in the red planet, only one specimen of JSC Mars-1 was compacted at 0% of moisture content.

The densification processes produced in the field are represented in the laboratory by the modified Proctor test. In the field, the energy of compaction in the is controlled by a given compaction equipment's weight, and the number of passes above a volume of cut or fill sections. Nevertheless, this method of compaction can be used to simulate density achieved as a result of impacts on the surface of Mars (Gabasova & Kite, 2018). However, since no compaction equipment is available on Mars, other methods of densification are studied that can better simulate field conditions on Mars.

For the modified Proctor test, the energy of compaction (CE) is calculated by using the following equation (ASTM D1557):

$$CE = \frac{(L \times B \times WH \times HF)}{V_M} \quad (7),$$

where L is the number of compacted layers; B is the number of impact blows; WH is the weight of the impact hammer (kN); HF is the hammer falling height (m); and V_M is the volume of the compaction mold (m^3).

The achieved dry density of JSC Mars-1, obtained with the modified Proctor test was of $1,158.2 \pm 16.0 \text{ kg m}^{-3}$. The applied compaction energy was of $2,693.3 \text{ (kN m/m}^3\text{)}$.

6.3 Vibratory Compaction

Allen et al. (1998) used vibratory methods of compaction in the laboratory to simulate field densification processes in Mars. Regolith materials subjected to vibration may reduce their void ratio by the collapse of pore space, and therefore, an increase in its dry density. The compaction process by the vibration is replicated in the laboratory with the maximum index density test (ASTM D4253). Also known as the shake table method, this test procedure utilizes a surcharge load appliance at the top of the soil specimen, which is confined in a calibrated mold. The test is performed while the entire assembly is subjected to vertical vibration for an amount of specific time.



Figure 14. Shake table equipment.

The shake table method provides a variety of achieved dry density values based on the amount of vibration time and the vertical vibration frequency. The vibration frequency is controlled with an incorporated rheostat. According to Arcement and Wright (2001), the energy of compaction (CE) involved in using the shake table is:

$$CE = \frac{EI \times RCap\% \times t \times L}{V_M} \quad (8).$$

where EI is the electrical input (W); $RCap\%$ is the rheostat capacity; t is the vibration time (s); L is the number of compacted layers; and V_M is the volume of the compaction mold (m^3).

An advantage of incorporating vibration in the compaction process is the concomitant rearrangement of particles, resulting in a reduced void ratio. However, excessive vibration may also result in segregation of coarse particles from fine particles. Figure 15 shows the density of JSC Mars-1 compacted at a variety of vibration efficiencies ($RCap\%$). For reference purposes, the measured minimum index density is included in this plot with a rheostat capacity of 0%, and an achieved dry density of $872.7 \pm 2.2 \text{ kg m}^{-3}$.

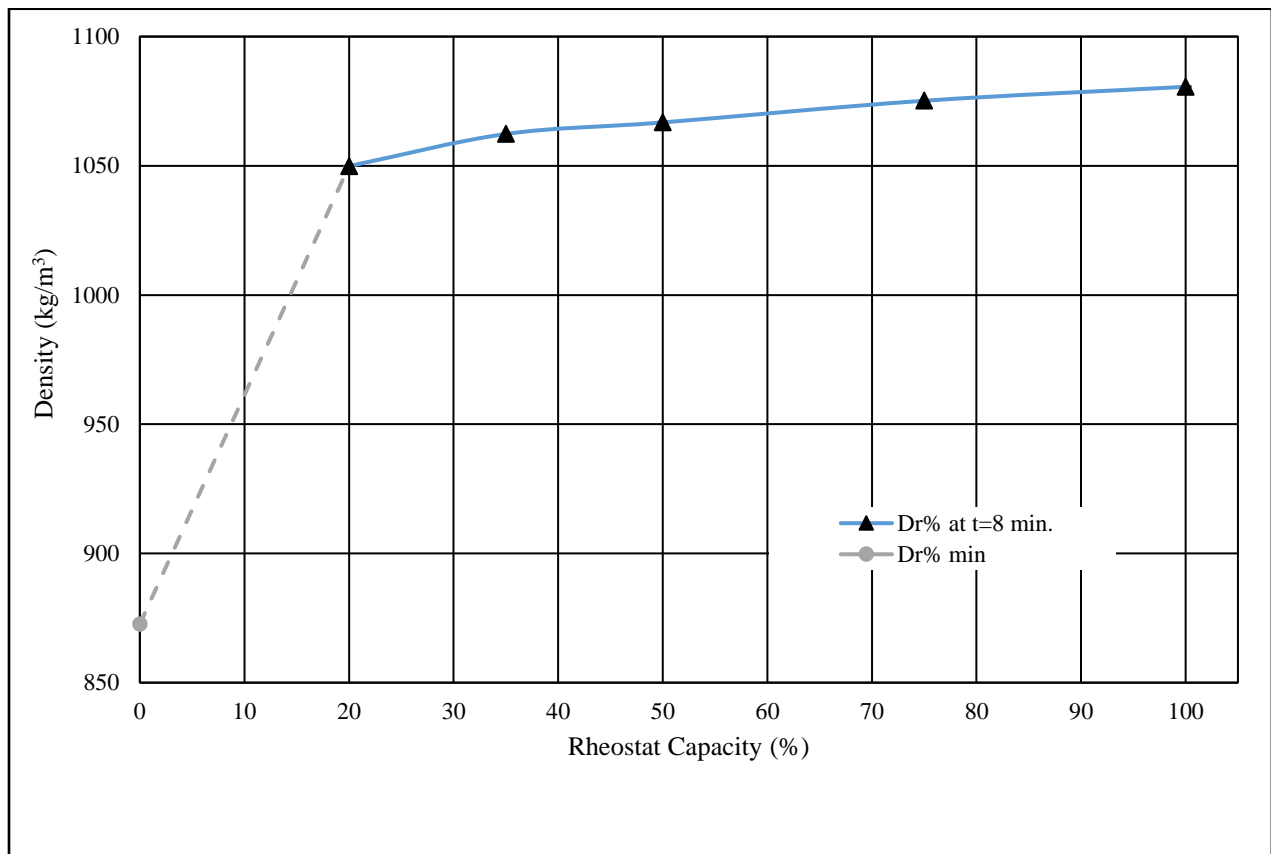


Figure 15. Maximum index density values achieved by vibration at different rheostat capacities, with respect to minimum index density ($Dr\% \text{ min}$).

The densification of JSC Mars-1 was also studied by using the British vibratory hammer method (ASTM D7382). The British vibratory hammer method does not apply a dead load at the top of the cross-sectional area of the specimen. The British vibratory hammer depends only on densification by vibration, but with a higher vibration efficiency than the shake table. The compaction energy applied by the British vibratory hammer can also be quantified by Equation 8 (Arcement & Wright, 2001).

A higher density was achieved for JSC Mars-1 using the British vibratory hammer compared to the shake table (Figure 16). A possible explanation for this is the variability of the respective compaction energy (*CE*) values. Table 11 provides a summary of the achieved dry densities in relation with the applied compaction energy values.

Table 11: Summary of Results for Compaction by Vibration Methods.

Compaction Method	Rheostat Capacity (%)	Dry Density (kg m⁻³)	Standard Deviation (kg m⁻³)	Compaction Energy (kN-m/m³)
Shake Table	20	1,049.9	0.9	4,068.3
	35	1,062.3	0.5	7,119.4
	50	1,066.8	3.9	10,170.6
	75	1,074.9	3.5	15,255.9
	100	1,081.4	4.4	20,341.3
British Vibratory Hammer	100	1,124.5	20.8	31,947.0

As shown in Table 11, the achieved dry density tends to increase as the compaction energy increases as well. This behavior was studied by Proctor (1933). His study consisted in the analysis of how the increase in compaction energy applied by impact compaction results in higher density values. However, this behavior is presented in compaction by vibration as well. The relationship

between achieved dry density and compaction energy applied by the British vibratory hammer and the shake table at different rheostat capacities, is presented below.

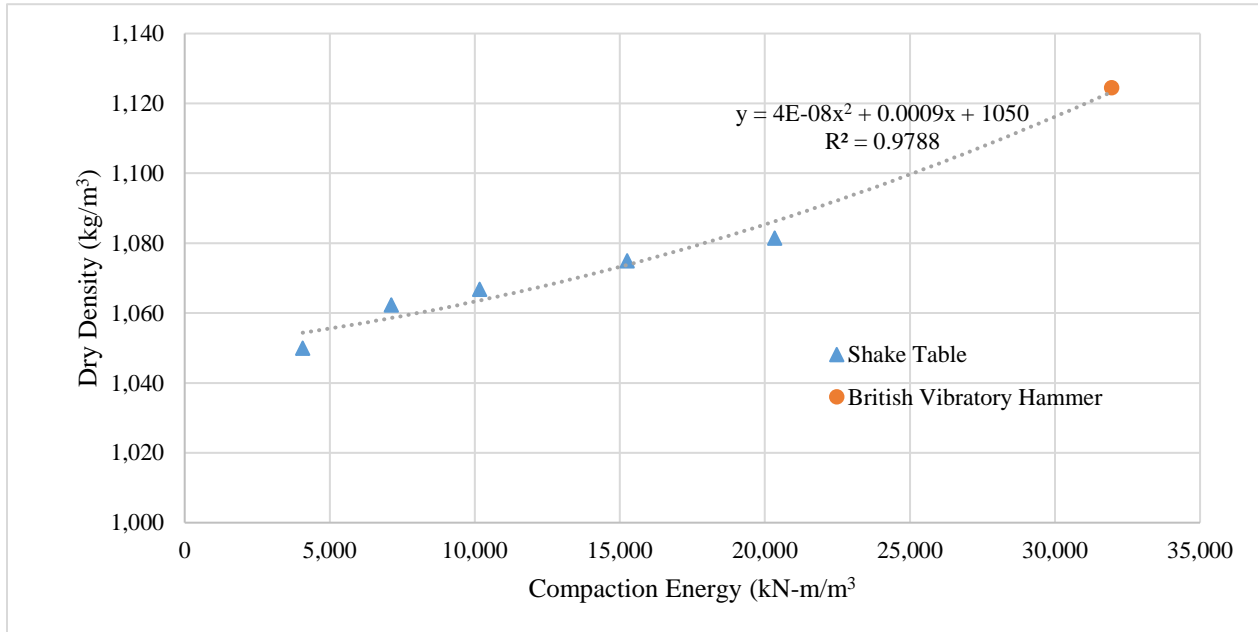


Figure 16. Maximum index density values achieved by vibration methods of compaction.

6.4 Gyrotory Compaction

Gyration methods of compaction are mostly used for hot-mix asphaltic concrete materials (Arabali et al., 2018). However, for completeness in this study of the effect that different methods of compaction have on the densification of JSC Mars-1, compaction by gyration is also considered. Compaction by gyration is affected by the following parameters:

- Normal pressure (σ_l , kPa): the amount of static pressure applied to the top of the soil specimen contained within a standardized mold.
- Gyration rate (Gr , revolutions per minute): the velocity at which the standardized mold rotates around its vertical axis.
- Angle of gyration (G^θ): the angle of the interior of the mold wall with respect to the bottom plate (Prowell, et al., 2003).

A set of gyratory compaction tests were performed on JSC Mars-1 using various values of Gr and σ_l . The results are summarized in Table 12.

Table 12: Gyratory Compaction Test Results

Normal Pressure (kPa)	Gyration Rate (RPM)	Change in Height ΔH (mm.)	Dry Density (kN/m³)	Compaction Energy (kN-m/m³)
206.8	5.0	4.38	932.3	13
	10.0	10.08	975.5	23
	30.0	8.14	964.3	25
	60.0	7.36	946.7	30
503.3	5.0	9.374	1,023.6	76
	10.0	10.50	1,052.4	85
	30.0	9.52	1,047.6	75
	60.0	9.39	1,030.0	75
799.8	5.0	10.56	1,090.9	141
	10.0	12.76	1,124.5	175
	30.0	11.91	1,118.1	163
	60.0	11.76	1,111.7	160

In total, 24 tests were performed to determine the optimum combination of compaction by gyration parameters that result in the highest dry density value of JSC Mars-1. Figure 13 shows the relationship between dry density (γ_{dry}) and GR , at three levels of σ_l . As shown in Figure 13, the governing parameter in the densification of JSC Mars-1 by gyratory compaction methods, is σ_l . Each curve represents the relationship of achieved dry density values and gyration rates, at the

same level of normal pressure. An increase of 150 kg m^{-3} in the dry density was achieved by increase the normal pressure from 206.8 kPa to 799.8 kPa. In contrast, the maximum increase of the dry density obtained as a result of the application of different gyration rates resulted in 43.2 kg m^{-3} . Therefore, the main parameter affected density in compaction by gyration is normal pressure.

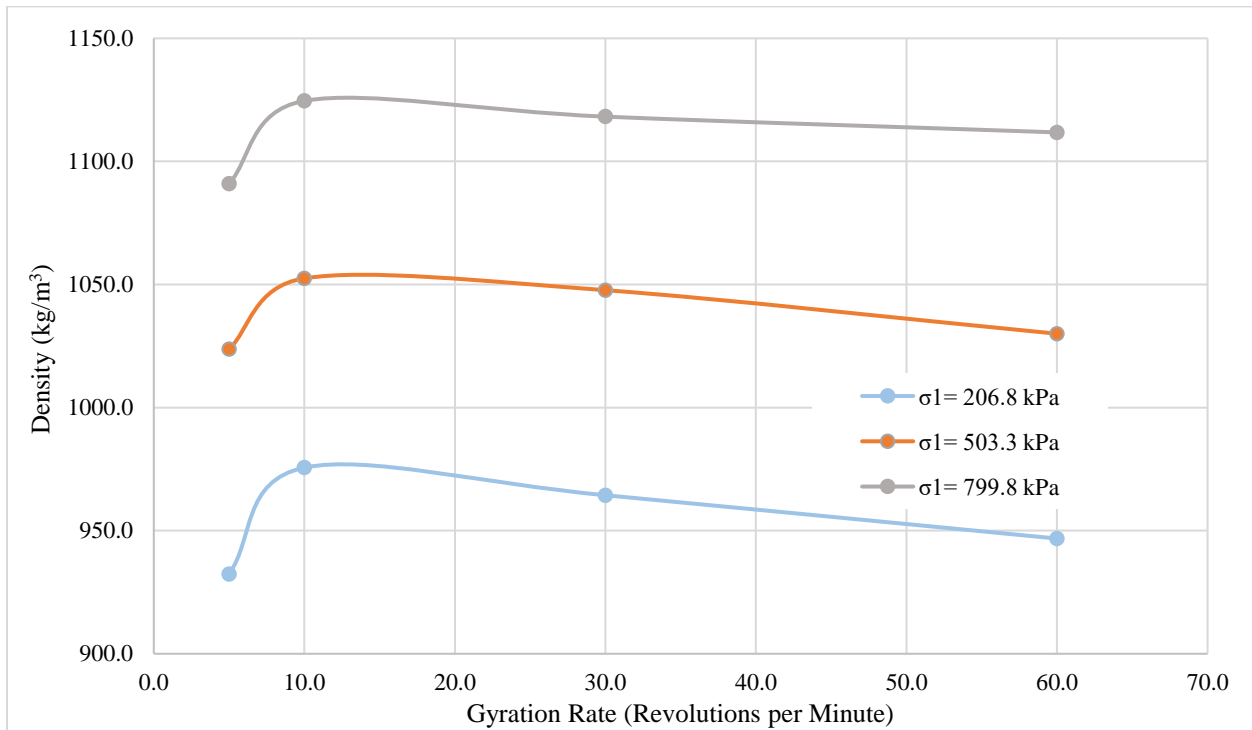


Figure 17. Dry density (kg m^{-3}) of JSC Mars-1 vs gyration rate (RPM).

Another important factor in the gyratory compaction JSC Mars-1 is *GR*. As shown in Figure 14, an optimum gyration rate is exhibited by all curves in terms of the achieved dry density values. A gyration rate of 10 revolutions per minute (RPM) has been determined as the optimum value for the three levels of normal pressure used. As the gyration rate increases above (or decreases below) the optimum value, the achieved dry density values tend to decrease. The compaction curve corresponding to the lowest normal pressure ($\sigma_1 = 10 \text{ kPa}$) exhibits the most visible peak. This means that the dry density values of JSC Mars-1 subjected to higher normal pressures are less dependent to gyration rates, as shown in the upper curve ($\sigma_1 = 799.8 \text{ kPa}$) in Figure 17.

The variation in density of JSC Mars-1 as a function of gyration rate is associated with segregation of the fine-grained particles with respect to the coarse-grained particles. As the gyration rate increases above the optimum value, the fine-grained particles tend to migrate to the specimen's outer regions as a result of the centrifugal forces involved. These forces are reduced as the confinement pressure increases which decreases the amount of segregation. This is why the peaks of the curves in Figure 17 are more visible at lower levels of confinement. On the other hand, as the gyration rate decreases below the optimum value, JSC Mars-1 tends to homogenize within the compaction mold. The fine-grained particles generated by crushing, due to the confinement pressure exerted, tend to re-accommodate in the void space between the coarse-grained particles, which results in an increase in the dry density of the specimen. This behavior occurs for the gyration rates that are lower than optimum values for the three curves. The compaction effort (E) for gyration is calculated as follows (Arabali et al., 2018):

$$CE = \frac{\sigma_1 \times \Delta H}{V_f} \quad (9).$$

where σ_1 is the normal pressure (kPa); ΔH is the change in the specimen's height (mm); and V_f is the final volume of the specimen (m^3).

6.5 Comparison of Compaction Methods

In total, 58 tests were performed to determine the compaction method that resulted in the highest dry density of JSC Mars-1. The modified Proctor test proved to be the best method of compaction (Figure 18). The British vibratory hammer and the gyratory compactor ($\sigma_s=799.8$ kPa, GR=10 RPM) had similar performance to one another. The relationship of the dry density values achieved by the methods of compaction with respect to compaction energy, is presented in Figure 15.

This work demonstrates that a linear relationship cannot be established for the maximum achieved dry density and energy of compaction for JSC Mars-1. Instead, a logarithmic relationship was established, as shown in Figure 18. An increase in the energy of compaction applied by the three methods of compaction does not necessarily mean that a highest dry density value will be obtained. The minimum index density value of JSC Mars-1 is used in Figure 18 to represent the increase of the dry density values achieved by each of the methods of compaction studied with respect to the minimum value.

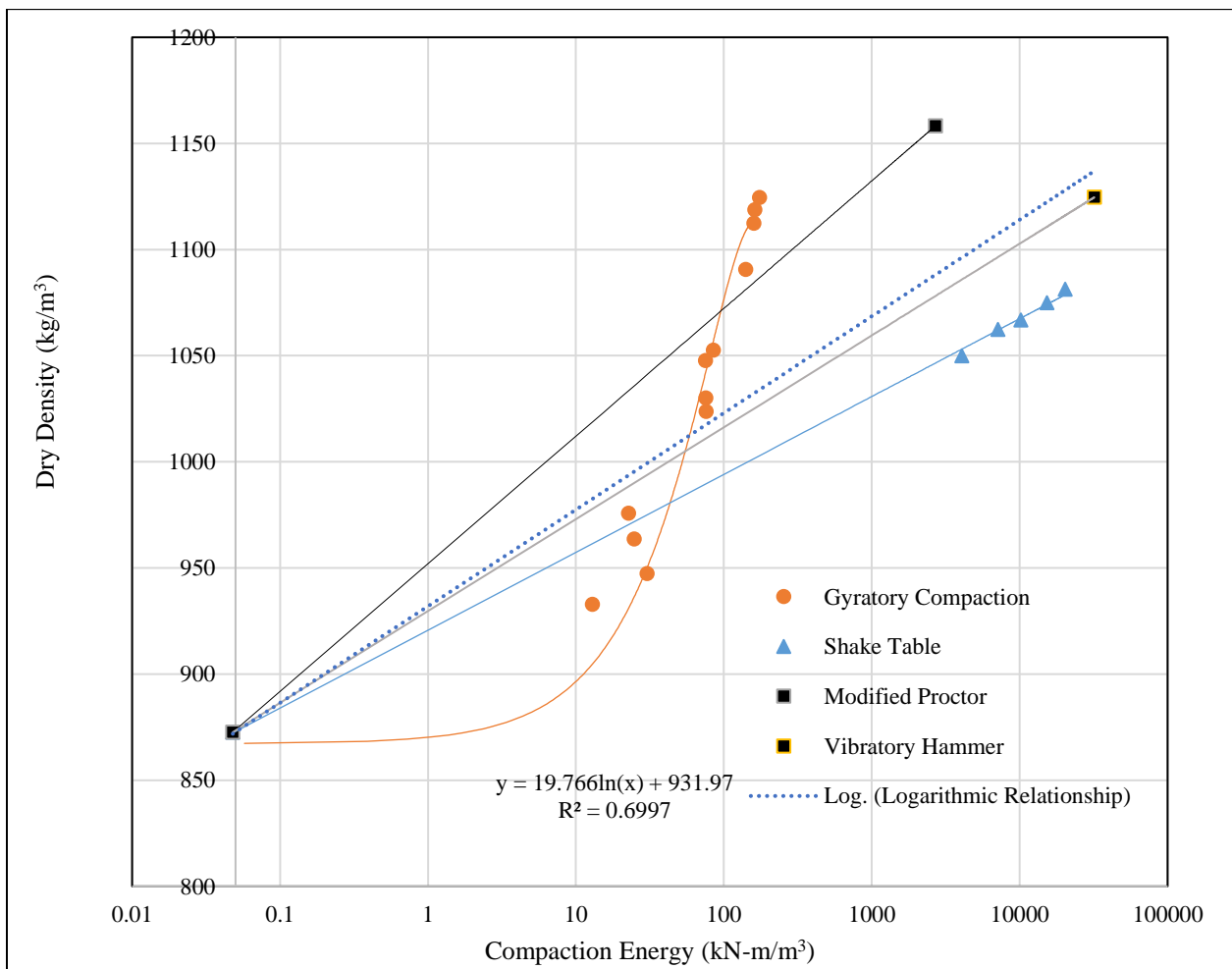


Figure 18: Dry density values of JSC Mars-1 obtained by using different methods of compaction.

As shown in Figure 18, the method with the highest energy of compaction is the British vibratory hammer method. However, this method did not result in the highest dry density. The method that resulted in the lowest degree of relative compaction was the shake table, even though it had the second-highest compaction energy. These observations suggest that an increase in the energy of compaction is not correlated with an increase in the maximum achievable dry density of JSC Mars-1. Compaction by gyration is an efficient method to increase the dry density of JSC Mars-1. This method requires a relatively low compaction effort as compared to compaction by vibration and impact (Figure 18). Compaction by gyration required only 6.50% of the energy required by the Proctor method to achieve 97% relative compaction.

Another critical behavior associated with each of the compaction methods used for JSC Mars-1 is particle breakage, or generation of fine-grained material. This phenomenon plays an essential role in densification of JSC Mars-1. For example, compaction using the British vibratory hammer and modified Proctor techniques resulted in a considerable amount of fine-grained particles (Table 13, Figure 16). This contributes to the increase of the dry density derived from the modified Proctor test, but not for the British vibratory hammer. The fines generated by the British vibratory hammer differs from the modified Proctor by 8%. Given that JSC Mars-1 is classified as poorly graded sand with silt (SP-SM), the generation of fines results in an increase of the dry density values. However, an excessive amount of fines generated may also result in low density values. In fact, generation of fines in the compaction process has a different impact in terms of dry density values obtained by vibratory and impact methods, as stated by Townsend (1972).

The generation of fines by the modified Proctor results in an increase of the dry density. In contrast, the compaction method that generated the smallest percentage of fines was the shake table (Table 13, Figure 19) This may be the main reason for the low density obtained by this

method compared to the other techniques. As stated in Chapter 3, JSC Mars-1 is classified as poorly graded sand with silt (SP-SM). Therefore, fine particles generated during compaction tests filled pore spaces present in the specimen. Pore space exists in the material (in the form of gaps between large grains) because it is poorly-graded. More pore space means lower density. However, if a process creates more fine-grained material in the specimen, that fine-grained component can fill pore spaces between larger grains. The result is an increase in density.

The JSC Mars-1 material remained by the compaction test was characterized with particle-size distribution curves and compared with the original curve provided in Chapter 1. The curves are presented in Figure 19.

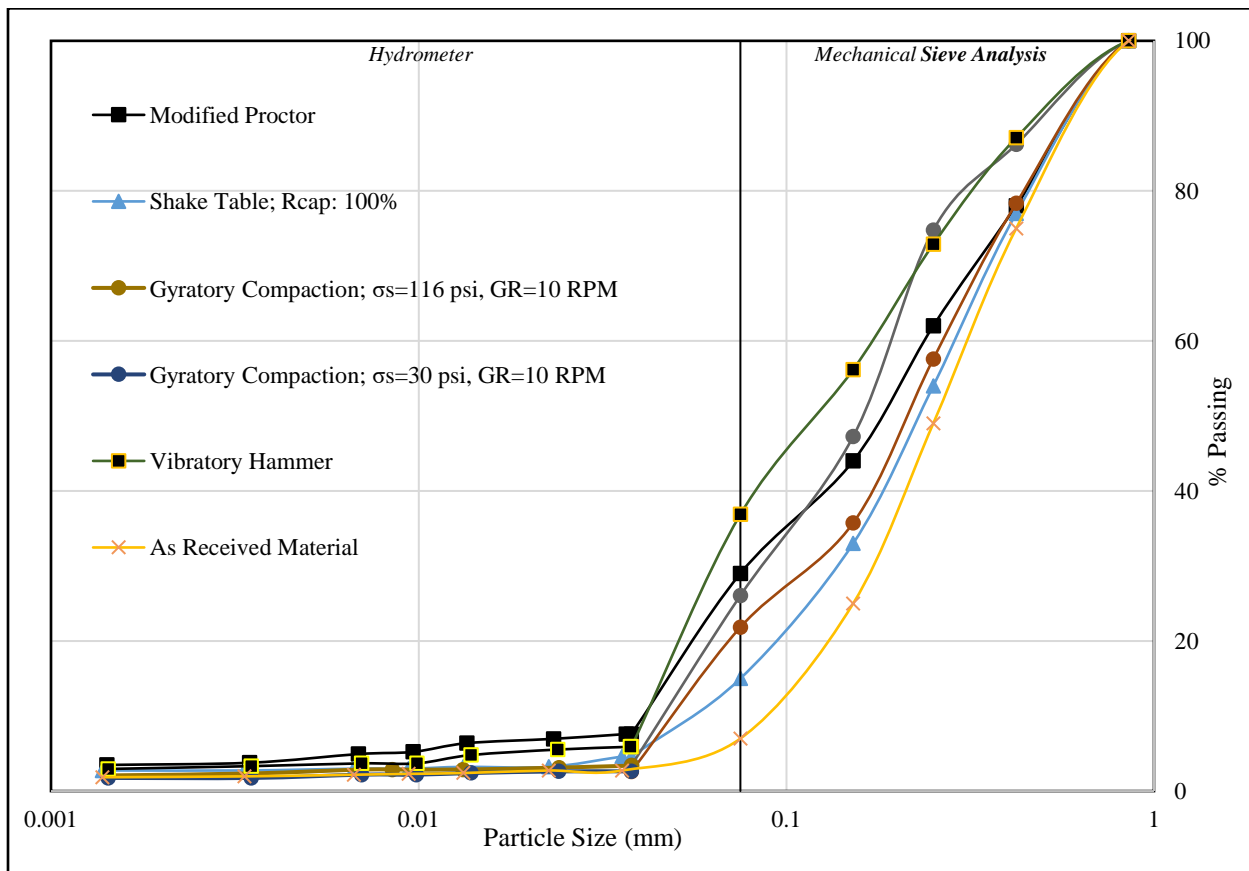


Figure 19. Particle size distribution curves developed with the material tested under different ASTM compaction standards.

Compaction using the British vibratory hammer applies more energy into the specimen and generates more fine particles (Figure 19). This combination of factors did not result in a dry density higher than that attained with the modified Proctor method due to segregation of fine-grained particles from coarse-grained particles caused by excessive vibration.

Table 13. Variation of Particle Size as a Function of Compaction Method and Associated Factors.

Particle Size	As Received Material	Shake Table (RCap= 100%)	Modified Proctor	Gyratory Compaction (σs: 206.8 psi, GR= 10 RPM)	Gyratory Compaction (σs: 799.8 psi, GR= 10 RPM)	Vibratory Hammer
Gravel Content %	0	0	0	0	0	0
Sand Content %	93	85	71	74	78	63
Silt Content %	5.1	12.3	25.4	23.8	19.8	33.9
Clay Content %	1.9	2.7	3.6	2.2	2.2	3.1

Table 13 summarizes particle sieve analyses of the material tested in each compaction method and it quantifies the variation of the relative concentrations of sand, silt, and clay particles present as a result of degradation. Indeed, according to Table 9, the concentration of clay-sized particles did not change as dramatically as the other size fractions did during the experiments.

CHAPTER 7: MECHANICAL PROPERTIES OF JSC MARS-1

7.1 Input Parameters

Starting from the premise that density plays a significant impact in the mechanical properties of geo-materials, a full laboratory experiment matrix (Table 3) was developed for the study of the compressibility and shear strength properties of JSC Mars-1, at four different initial relative compaction values. The minimum relative compaction value, 75.4%, corresponds with the ratio of the minimum index density (Section 6.1) and the maximum dry density. Furthermore, the dry density value of $1,158.2 \text{ kg m}^{-3}$ was used as a relative compaction value of 99%. The remaining 1% was considered due to the standard deviation of 16.0 kg m^{-3} , obtained by the modified Proctor. Two additional relative compaction values, 91.8% and 86.3%, were used as well. These values were obtained based on equal increases of the minimum relative compaction towards the maximum relative compaction.

7.2 Compressibility

Compressibility is defined as the dissipation of pore spaces, which results in an increase of density. Similar to compaction, compression of geo-materials is a method of densification. However, compression differs from compaction in terms that it may occur in a natural manner, without the usage of any compaction equipment.

In total, nine 1-dimensional compressibility tests (ASTM D2435) were performed on JSC Mars-1 to study the variability of the compressibility characteristics as a function of initial degree of relative compaction. Figure 20 shows the behavior of JSC Mars-1 subjected to a sequence of incremental static loads at different initial relative compaction values. A load increment ratio of 2 was used for this 1-dimensional compressibility test of JSC Mars-1, as specified by ASTM D2435.

An initial axial effective stress value of 13.8 kPa was used to simulate the stress induced by the Viking I landing gear footpads (Moore et al., 1987) on the martian surface.

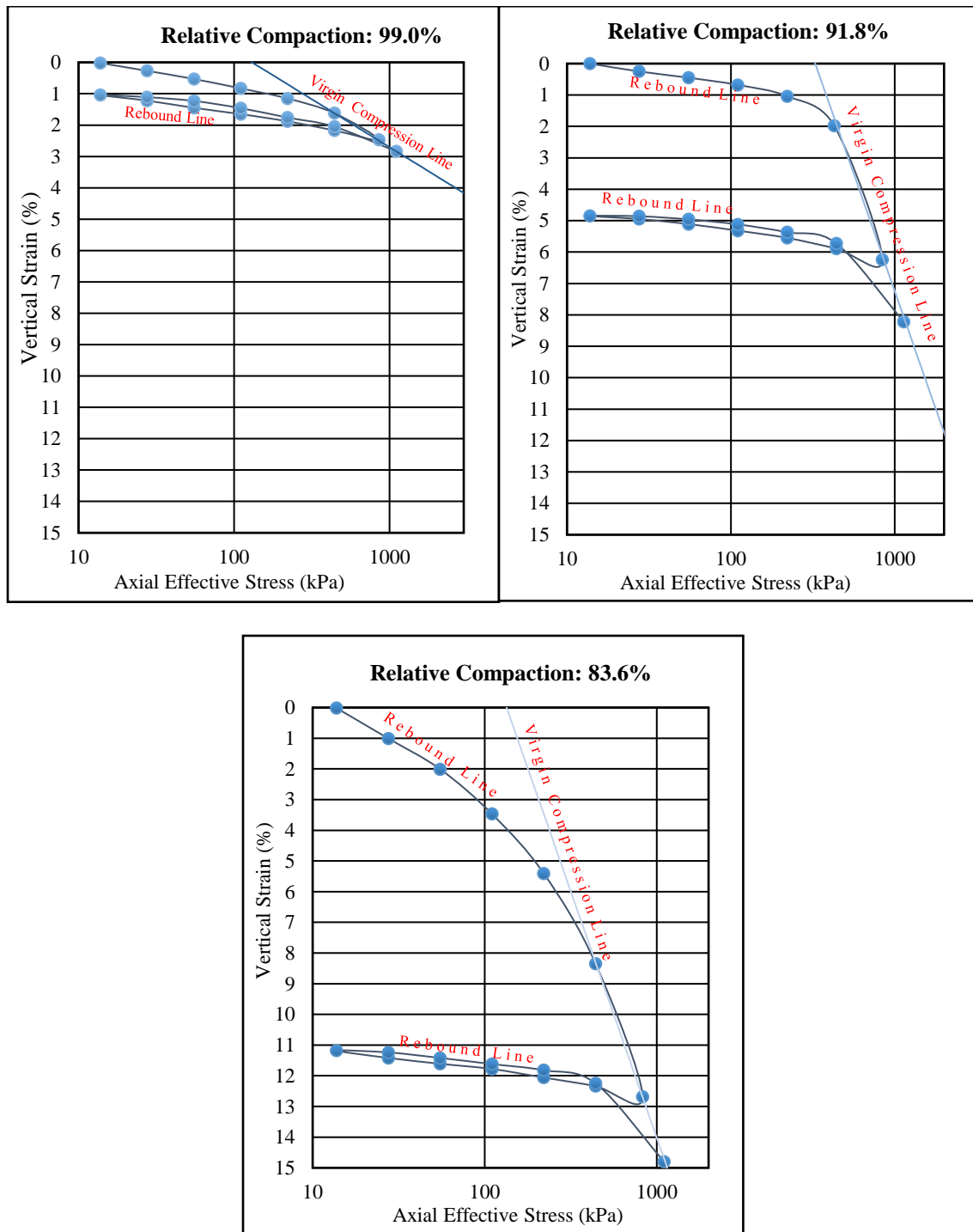


Figure 20. Compression curves (axial effective stress in logarithmic scale) for JSC Mars-1 corresponding to different initial relative densities (expressed as percent relative compaction).

To determine the compressibility characteristics of JSC Mars-1, the relationship between axial effective stress and vertical strain was characterized. The JSC Mars-1 specimens were compacted at 99.0%, 91.8, and 83.6% of relative compaction. A pneumatic consolidation load frame was used to apply the axial effective stresses. The experiment was repeated twice to obtain accurate test results.

Three scenarios are presented in Figure 20. Apart from the different initial relative density values, all other test conditions are the same in each scenario: a load increment ratio of 2; an initial axial effective stress of 13.8 psi; and a final axial effective stress of 1,137.6 psi. Figure 20 provides an illustration of the compressibility characteristics of JSC Mars-1 at three initial degrees of initial relative compaction.



Figure 21. Pneumatic consolidation load frame used for the compressibility testing of JSC Mars-1.



Figure 22. JSC Mars-1 in the consolidation ring.

In soil mechanics, the virgin compression line (Figure 20) is the ideal relationship between the logarithm of the axial effective stress and the amount of vertical deformation for a given material, this deformation must bring a reduction in the soil volume (Liu & Carter, 1999). In the other hand, the rebound curve is defined as the relationship between the logarithm of the axial effective stress and the amount of vertical expansion of a given soil (Liu & Carter, 1999)..

Slopes of the virgin compression curve and the rebound portion of the compression curves are measured by the coefficient of volume compressibility (M_v) and the rebound index (C_s), respectively. The coefficient of volume compressibility is calculated as follows:

$$M_v = \frac{|\Delta\varepsilon_z|}{\log(\Delta\sigma_z)} \quad (10),$$

where M_v is the coefficient of volume compressibility in terms of axial strain; ε_z is the axial strain; and σ_z is the axial effective stress.

Furthermore, the rebound index is calculated with the following equation:

$$C_s = \frac{|\Delta\varepsilon_z|}{\log(\Delta\sigma_z)} \quad (11),$$

where C_s is the rebound index in terms of axial strain; ε_z is the axial strain; and σ_z is the axial effective stress.

It is important to note that the axial strain and axial effective stress values used for the calculation of the rebound index need to be obtained from the rebound portion of the curve. Whereas, the axial strain and axial effective stress values used for the calculation of the coefficient of volume change need to be obtained from the virgin portion of the curve.

The coefficient of volume compressibility defines the susceptibility of regolith to be deformed. If the slope of the virgin compression line is steep, it means the soil is highly deformable. The slope of the virgin compression curve corresponding to the JSC Mars-1 specimen with initial relative compaction of 99% is relatively flat. In contrast, the slope of the virgin

compression line of the JSC Mars-1 with an initial relative compaction of 83.6%, is relatively steep. As shown in Figure 20, the slope of the virgin curves of JSC Mars-1 tends to increase as the initial relative compaction decreases. In other words, since the pore spaces are larger, specimens with low initial relative densities have higher coefficients of volume change.

Another parameter that is affected by the variability of initial density is the pre-compression pressure (σ'_p). Referred to as maximum past pressure, this soil property provides an indication of the maximum stress that a soil specimen has sustained on its history in the field. In the compression curve, the pre-compression pressure value is considered as the boundary between the rebound and the virgin segments of the curve (Figure 20). For geo-structural design purposes, σ'_p is important for predicting settlement potential as well as non-homogeneous deformation of soils (Hammam et al., 2015). The σ'_p value is also affected by variation in initial density of soil specimens. Table 14 summarizes results for the set of compressibility tests performed on JSC Mars-1.

Table 14. 1-Dimensional Compressibility Tests: Summary of Results

Soil Parameter	Relative Compaction 99.0%		Relative Compaction 91.8%		Relative Compaction 83.6%	
	Avg. Value	Std. Dev.	Avg. Value	Std. Dev.	Avg. Value	Std. Dev.
Coefficient of Volume Compressibility (M_v)	0.006	0.0012	0.0234	0.0002	0.0246	0.0016
Rebound Index (C_s)	0.68	0.0004	0.67	0.0001	0.73	0.0003
Pre-compression Pressure (σ'_p , kPa)	399.9	13.8	379.2	34.5	172.4	13.8

Table 14 shows changes in volume of JSC Mars-1 are highly affected by the degree of initial relative compaction. Compared to the specimen prepared at 99% relative compaction which had a coefficient of volume compressibility of 0.006, the coefficient of volume compressibility increases to 24.4% for the specimen with an initial relative compaction of 83.6%. In contrast, the pre-compression pressure value for the specimen compacted at 83.6% of initial relative compaction, is reduced by 60% with respect to the pre-compression pressure at 99% of relative compaction, 399.9 kPa. On the other hand, the rebound index does not vary considerably among the three scenarios (Table 14). There are several possible explanations for this. One possibility is that, in the absence of hygroscopic moisture in the system, a swelling behavior cannot take place. Furthermore, the particle crushing behavior (Section 6.5) of JSC Mars-1 results in poor rearrangements of the particles. In other words, the removal of the axial load exerted over the specimens does not represent a swelling response of the material due to the absence of moisture, and due to the crushing of the coarse-grained particles.

7.3 Shear Strength

A series of direct shear tests were conducted in accordance with ASTM D3080. The input parameters used for the characterization of the shear strength properties of JSC Mars-1 are provided in Table 15.

Table 15. Direct Shear Test: Input Parameters

Initial Relative Compaction (RC%)	Deformation Rate (SR, mm min⁻¹)
75.4	0.4
83.6	1.9
91.8	7.6
99.0	-

The deformation rates correspond with the highest and lowest displacement, and an intermediate value of the capacity of the direct shear equipment used (Figure 23).



Figure 23. Direct shear test equipment.

In total, 18 specimens of oven-dried JSC-Mars 1 were prepared following the raining technique to achieve the minimum index density of $872.7 \pm 2.2 \text{ kg m}^{-3}$ (see Chapter 6). The JSC Mars-1 material was oven dried at $110 \pm 5 \text{ C}^\circ$ for 24 hours previous to specimen's preparation. An additional amount of 18 specimens with a relative compaction of 83.6% were also prepared using the raining technique. In addition, 36 specimens with initial relative compaction values of 91.8% and 99% were prepared by tamping the top of each specimen until the required relative compaction values were achieved.

In total, 72 direct shear tests were conducted for specimens with the input parameters described in Table 15. An additional amount of 73 tests were performed as replicates. Mohr-Coulomb failure envelopes (Figures 24-26) were constructed in accordance with ASTM D3080 to determine the variability of the cohesion (c) and angle of internal friction (ϕ°) parameters as a function of the rate of deformation and initial relative density. Figures 10-12 also show the shear stress vs. horizontal deformation curves at the three initial relative compaction values and the six

levels of confinement pressure used in the experiments. The deformation rate in Figures 24-26 is 7.62 mm per minute.

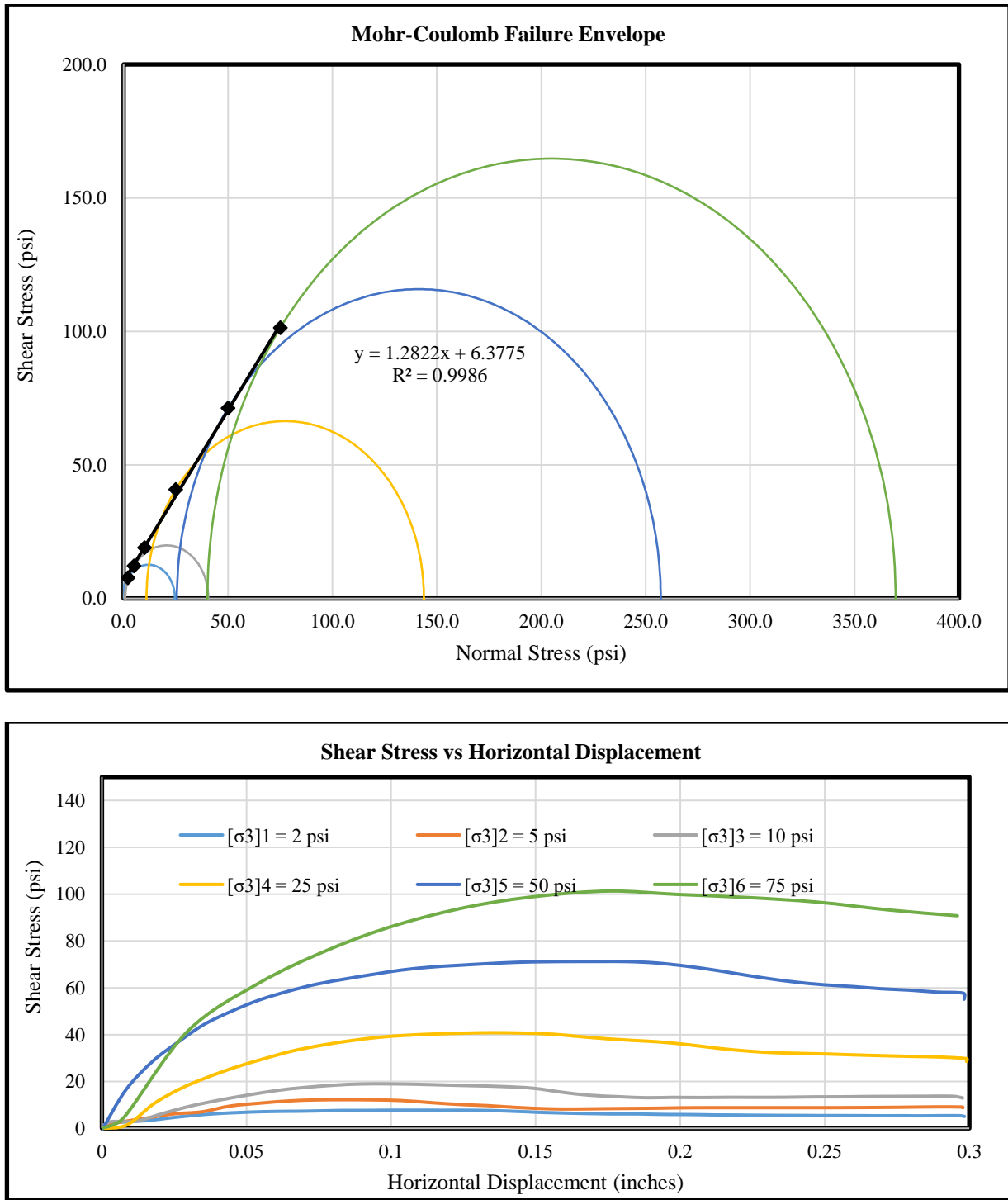


Figure 24. Mohr-Coulomb failure envelope (top) and shear stress vs. horizontal displacement relationship (bottom) for RC= 99% and SR=7.62 mm/minute.

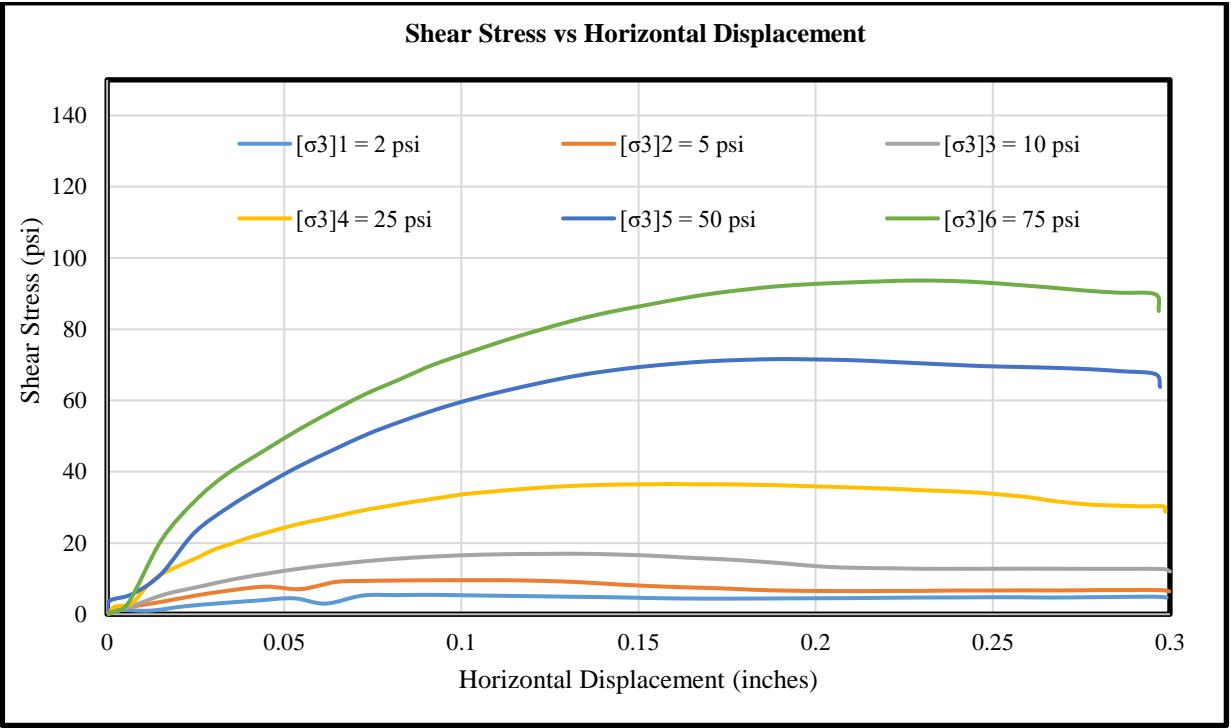
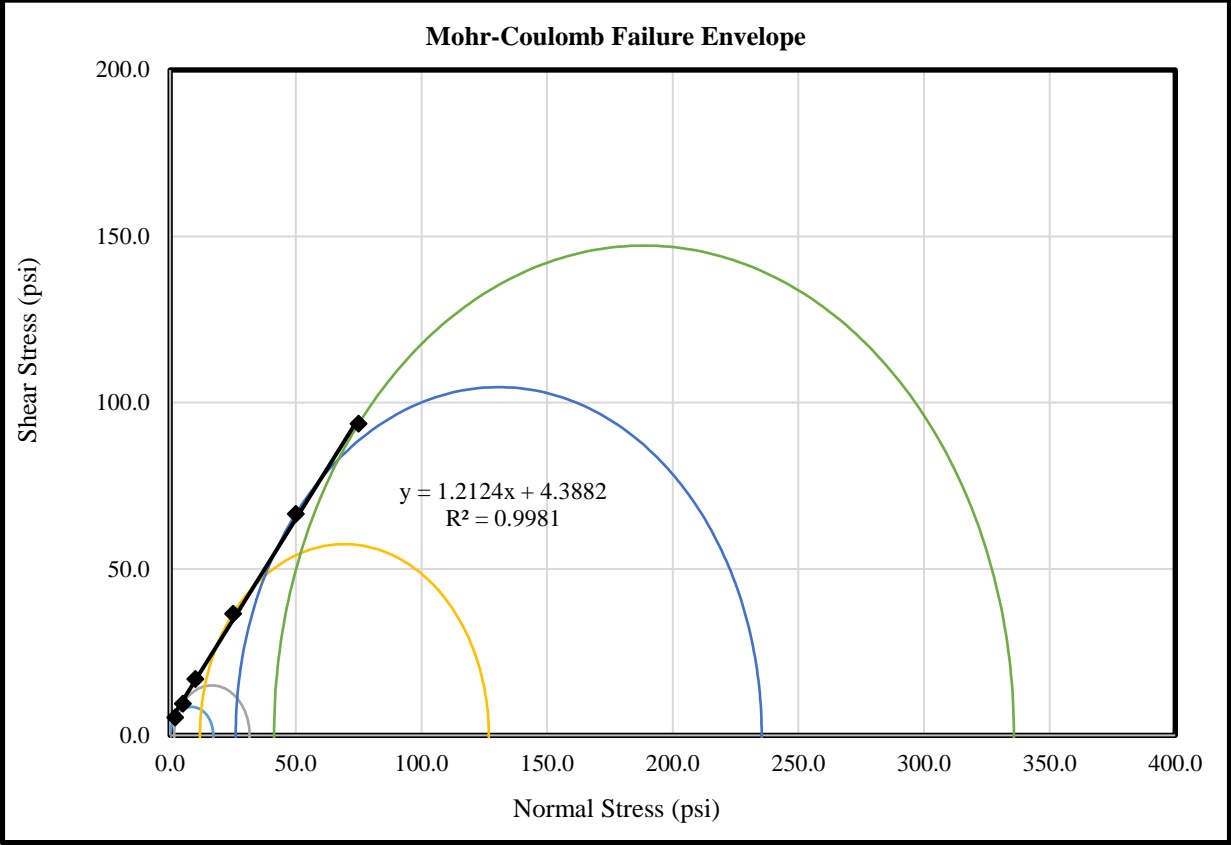


Figure 25. Mohr-Coulomb failure envelope (top) and shear stress vs. horizontal displacement relationship (bottom) for RC= 91.8% and SR=7.62 mm/minute.

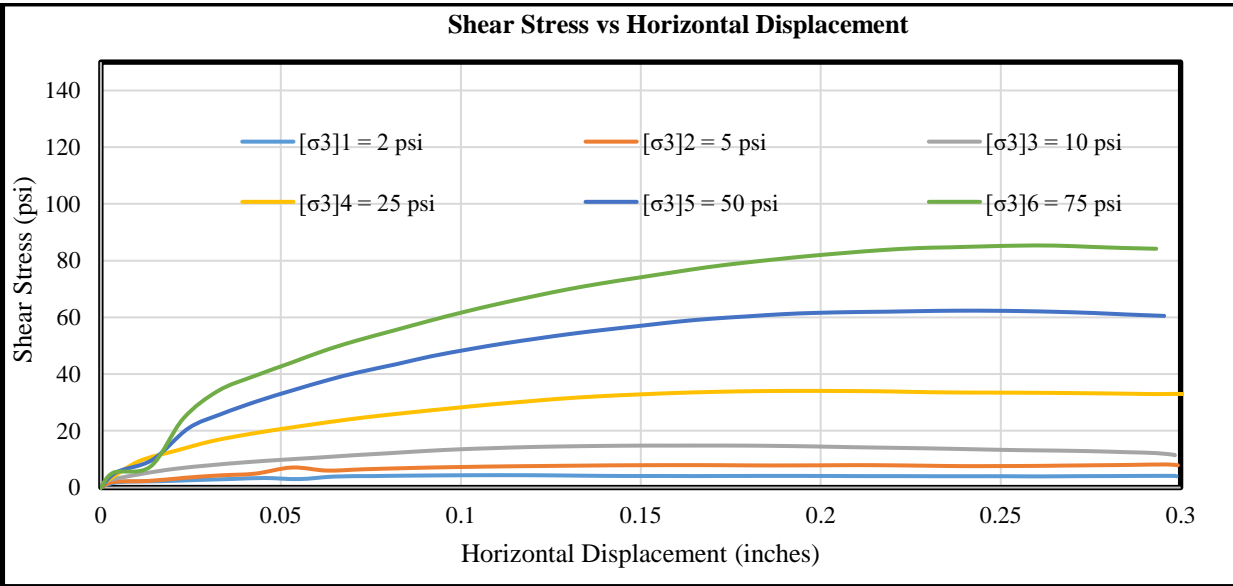
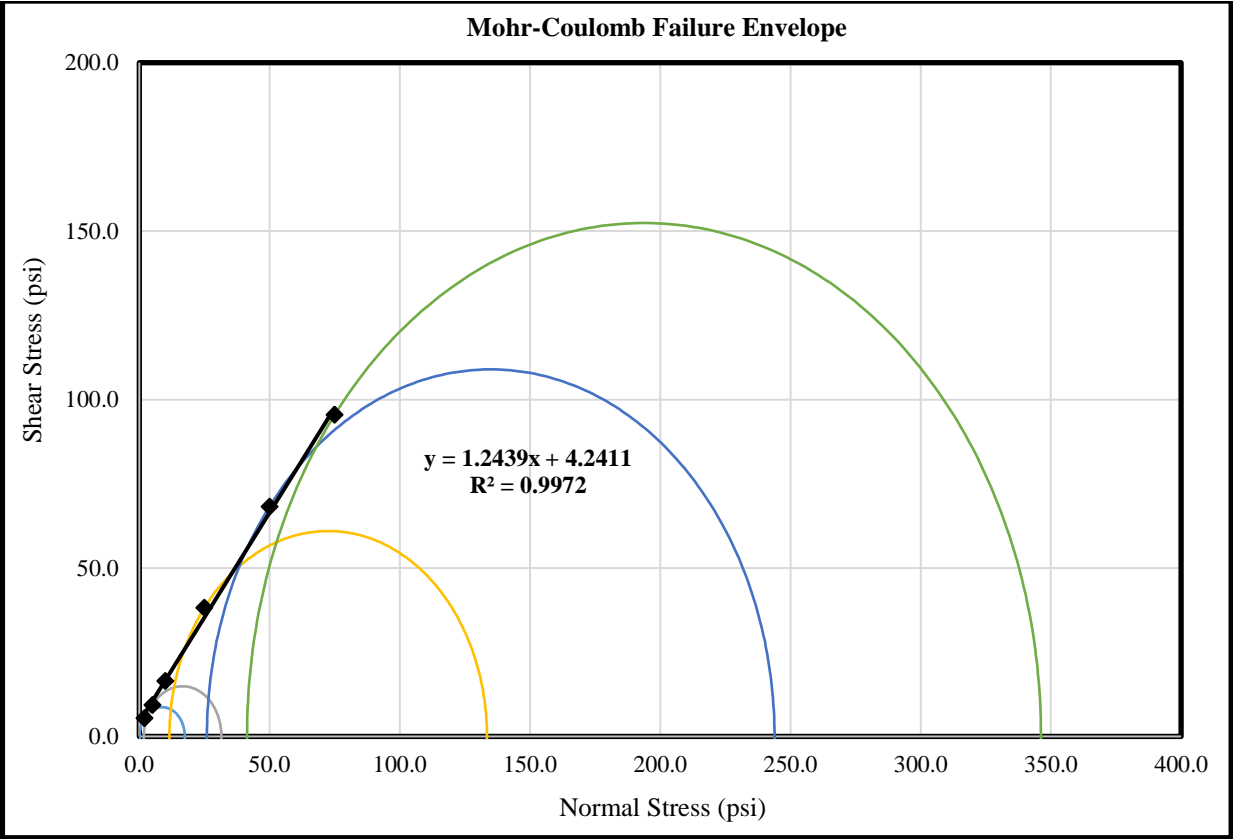


Figure 26. Mohr-Coulomb failure envelope (top) and shear stress vs. horizontal displacement relationship (bottom) for RC= 83.6% and SR=7.62 mm/minute.

The cohesion, angle of internal friction, and shear strength were computed from the Mohr-Coulomb failure envelopes (Figures 24-26) using the following equations (Poulos, 1971):

$$\text{Shear Strength } (\tau): \quad \tau = c + \sigma_N \tan (\varphi^\circ) \quad (12);$$

$$\text{Cohesion } (c): c = y - \text{intercept on the } \sigma\text{-}\tau \text{ plane} \quad (13);$$

$$\text{Angle of internal friction } (\varphi^\circ): \varphi^\circ = \tan^{-1} \left(\frac{\tau_{\max} - c}{\sigma_N} \right) \quad (14),$$

where τ_{\max} (kPa) is the maximum shear stress and σ_N is the normal stress (kPa)

Table 15 and Figure 27 summarize how cohesion (c , kPa), angle of internal friction (φ°), and shear strength (τ , kPa) vary as a function of relative compaction ($RC\%$) and deformation rate (SR , mm./min.).

Table 16. Shear Strength Properties of JSC Mars-1

SR	RC: 75.4%			RC: 83.6%			RC: 91.8%			RC: 99%		
	φ°	c	τ									
0.4	46.7	15.2	562.9	47.4	24.8	587.7	50.0	30.3	646.3	51.7	44.1	698.0
1.9	47.0	15.2	569.8	47.6	29.6	595.3	49.5	39.3	644.2	50.7	44.1	675.2
7.6	48.8	2.8	593.2	49.6	13.1	620.1	50.6	28.9	658.0	52.4	46.2	717.2

Each of the relationships presented in Figure 27 were constructed based on the output parameters obtained from the Mohr-Coulomb failure envelopes. These parameters, cohesion and angle of internal friction presents a variability depending on the initial degrees of relative compaction and strain rate values. In general, JSC Mars-1 exhibits low cohesion values due to the low concentration of fine-grained particles. Cohesive strength of geomaterials is directly associated with its plasticity behavior. Chapter 3 describes the absence of plasticity and fine-grained particles in JSC Mars-1. However, due to the generation of silt- and clay-sized particles in

the consolidation process of the direct shear test, particularly for specimens with high initial relative density, the cohesive strength values tend to increase as the initial relative density of the material increases.

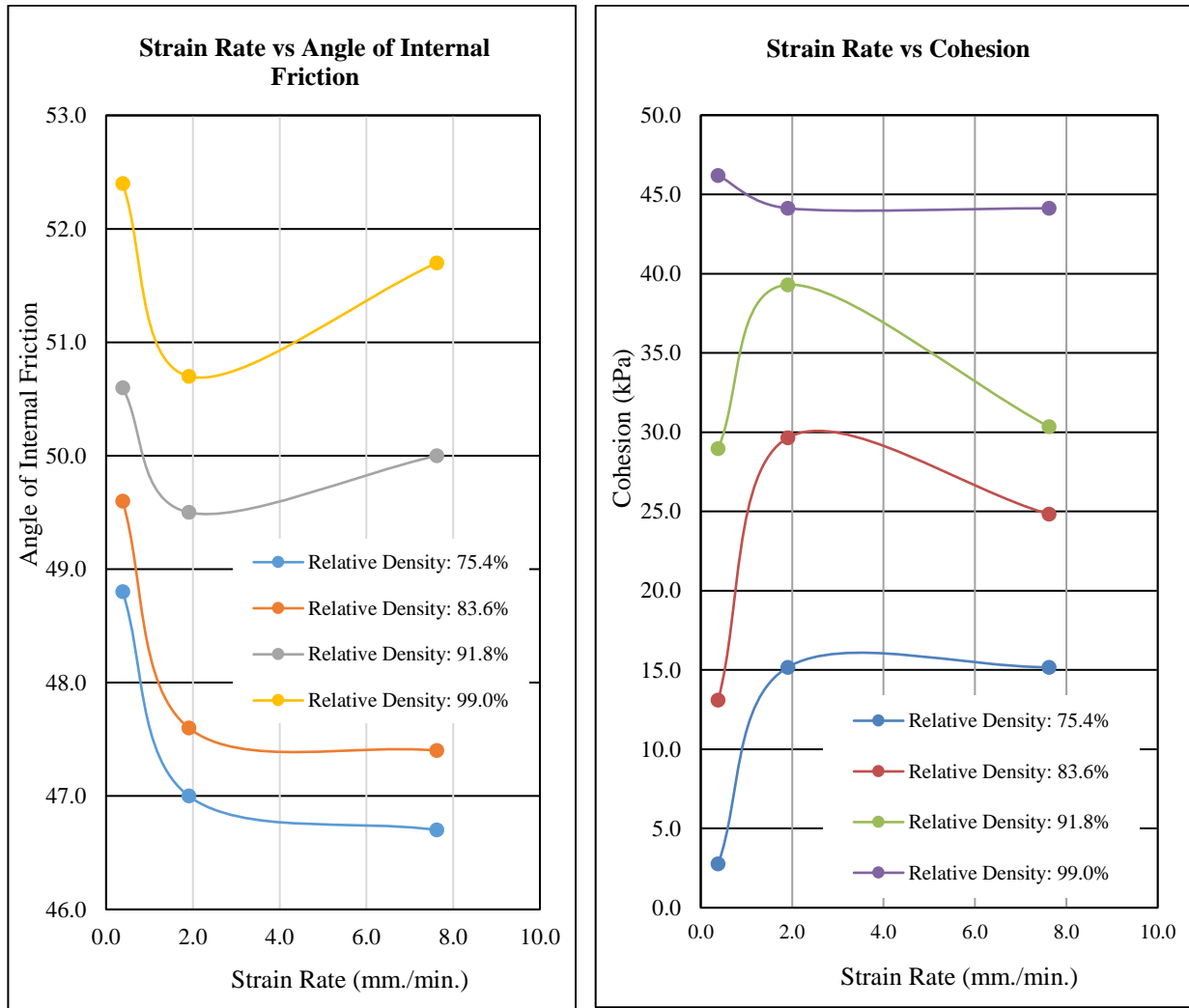


Figure 27. Angle of internal friction and strain rate (left) and cohesion and strain rate (right) relationships.

The rate of deformation certainly also plays an important role in the variability of cohesion properties. Figure 27 (right side) shows plots corresponding to initial relative compaction values of 75.4%, 83.6%, and 91.8% that present a visible peak at a strain rate of 1.9 mm/minute. In contrast, material compacted to a relative compaction of 99% are not susceptible to variation in

the rate of deformation at all due to its high relative compaction value. Figure 28 shows the remains of a specimen of JSC Mars-1 extracted from the direct shear mold after a test run with an initial relative density of 99%. The high cohesion in this material is obvious by the way it clumps together.



Figure 28. Remains of JSC Mars-1 after direct shear test experiment.

The angle of internal friction of JSC Mars-1 is relatively high compared to other terrestrial materials. A possible explanation for this is the high angularity index that this material has, which enhances the particle interlocking effect (see Chapter 4). Figure 27 (left side) shows plots that illustrate the variation of angle of internal friction with the rate of deformation.

Another important aspect that is worth highlighting is the slopes of the relationships corresponding to the cohesion and angle of internal friction parameters. Curves corresponding to the cohesion have a positive slope, while the ones corresponding to the angle of internal friction have a negative slope. Particle crushing behavior is a possible explanation for this phenomenon. It

is well known that the shear strength of fine-grained soils is associated with cohesion forces, while the angle of internal friction is the main parameter that contributes to the shear strength of coarse aggregate (Poulos, 1971). The generation of fines in the studied specimens of JSC Mars-1 promotes the cohesive increases in shear strength.

However, these fine particles reduce the angle of internal friction in two ways. First, the angularity index tends decrease due to the breakage of the coarse aggregate edges and the resulting increase in sphericity. Second, the generated fines tend to act as a lubricant between the remaining coarse particles, therefore, reducing the angle of internal friction.

To conclude, JSC Mars-1 has a high angle of internal friction and low cohesion, as predicted by the hydrometer test, Atterberg limits (Section 3.2), and angularity index (Section 4.1). However, the particle crushing behavior at high relative density values (Section 6.5) results in a decrease of the mechanical properties of JSC Mars-1.

7.4 Dilation Behavior

Geomaterials subjected to triaxial loads exhibit two types of behaviors: dilation and compaction (Chen & Kutter, 2009). The angle of dilation (Ψ^d) is a soil parameter that quantifies the tendency of granular soils to increase their volume as result of a combination of normal and shear stresses (Chen & Kutter, 2009). These behaviors are associated with the magnitude of the confinement pressure exerted in the material, and the particle's angularity index (Section 4.1).

Vertical deformation vs. horizontal displacement relationships were plotted from the data obtained from the series of direct shear tests conducted on JSC Mars-1. The angles of dilation for each of the scenarios resulted from the combination of normal pressures, initial relative compaction, and rates of deformation were calculated based on the vertical deformation vs horizontal displacement relationships.

The equation is presented below (Chen & Kutter, 2009):

$$\Psi^\circ = \tan^{-1}\left(\frac{\varepsilon_y}{\varepsilon_x}\right) \quad (15),$$

where ε_y is the vertical deformation corresponding to the steepest slope of the relationship and ε_x is the horizontal displacement corresponding to the steepest slope of the relationship.

Figures 29-33 present the vertical deformation vs. horizontal displacement relationships obtained for four values of initial relative compaction and rates of deformation (Table 15)

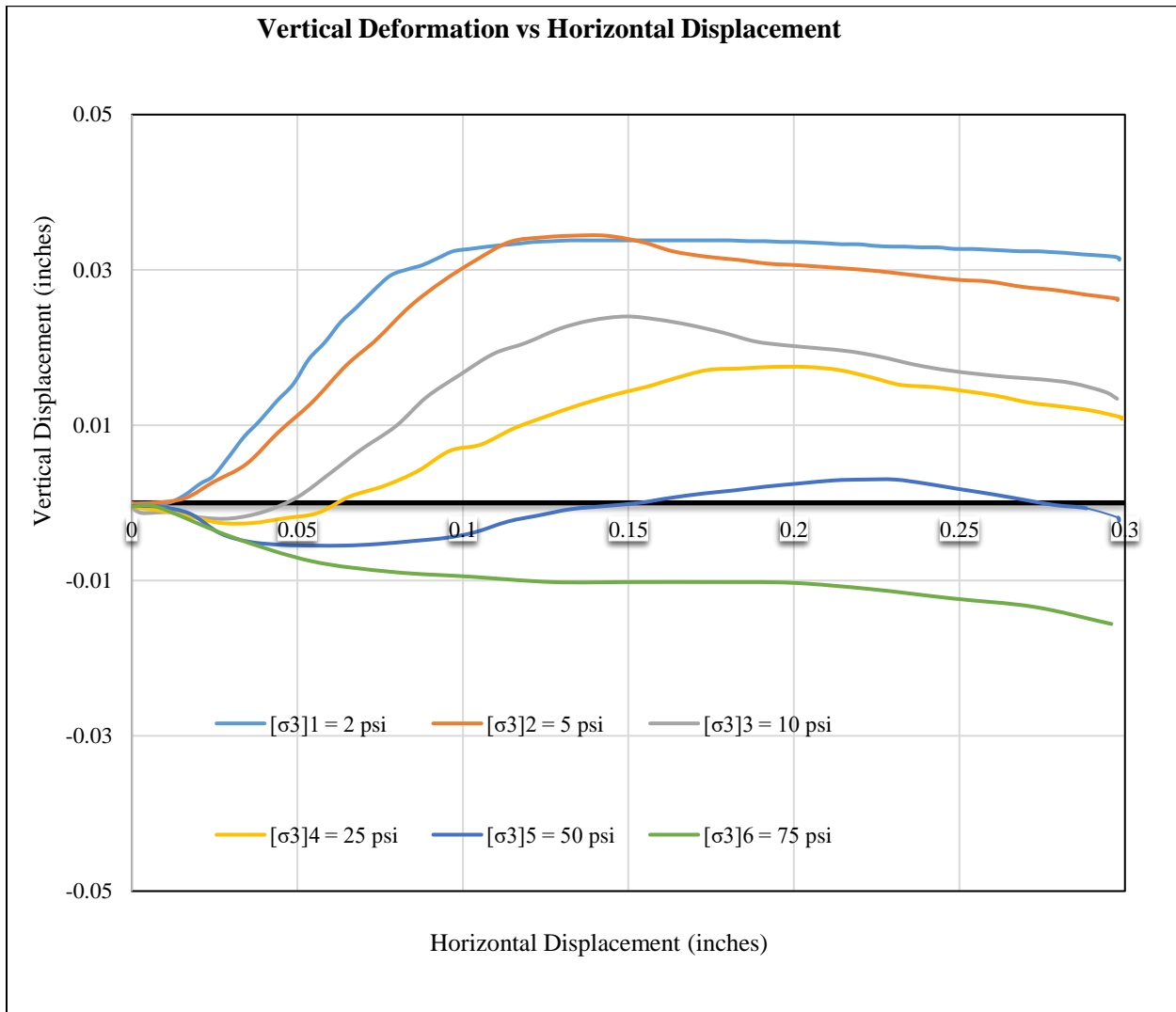


Figure 29. Vertical deformation vs. horizontal displacement relationship for RC=99.0%, SR=7.62 mm/min.

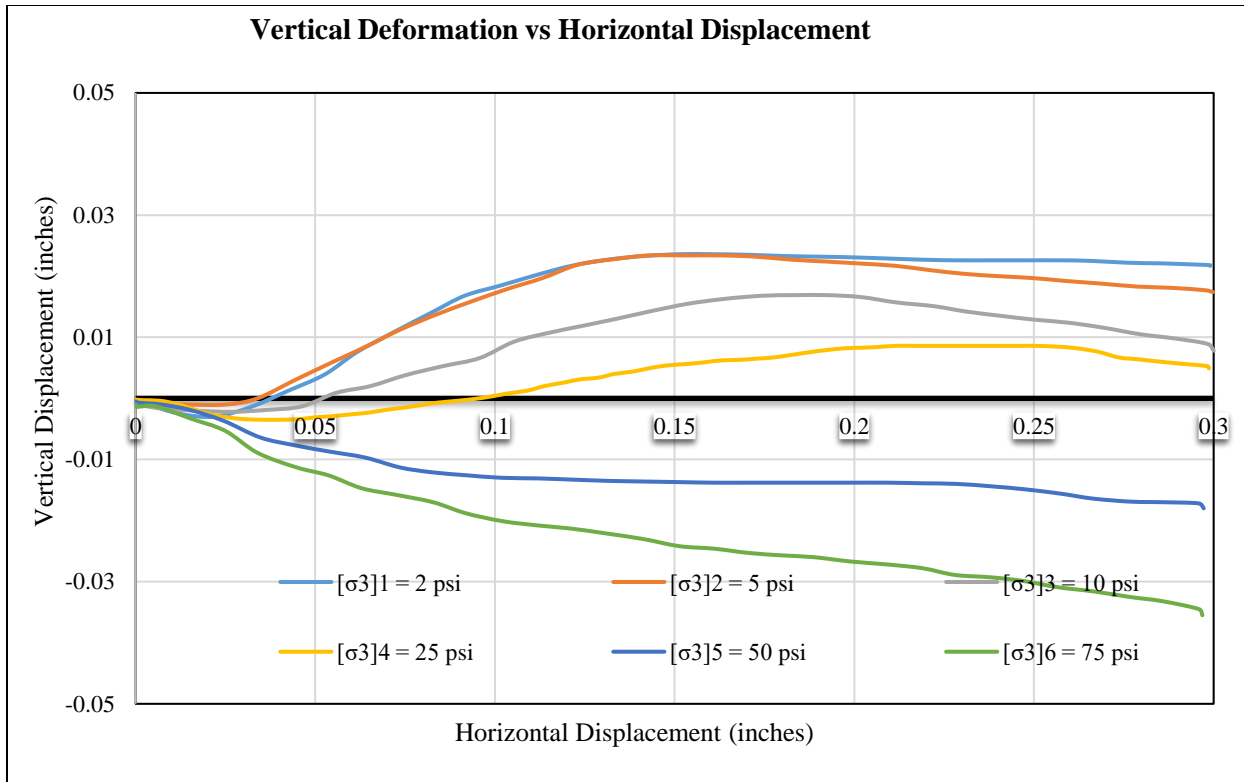


Figure 30. Vertical deformation vs. horizontal displacement relationship for RC=91.8%, SR=7.62 mm/min.

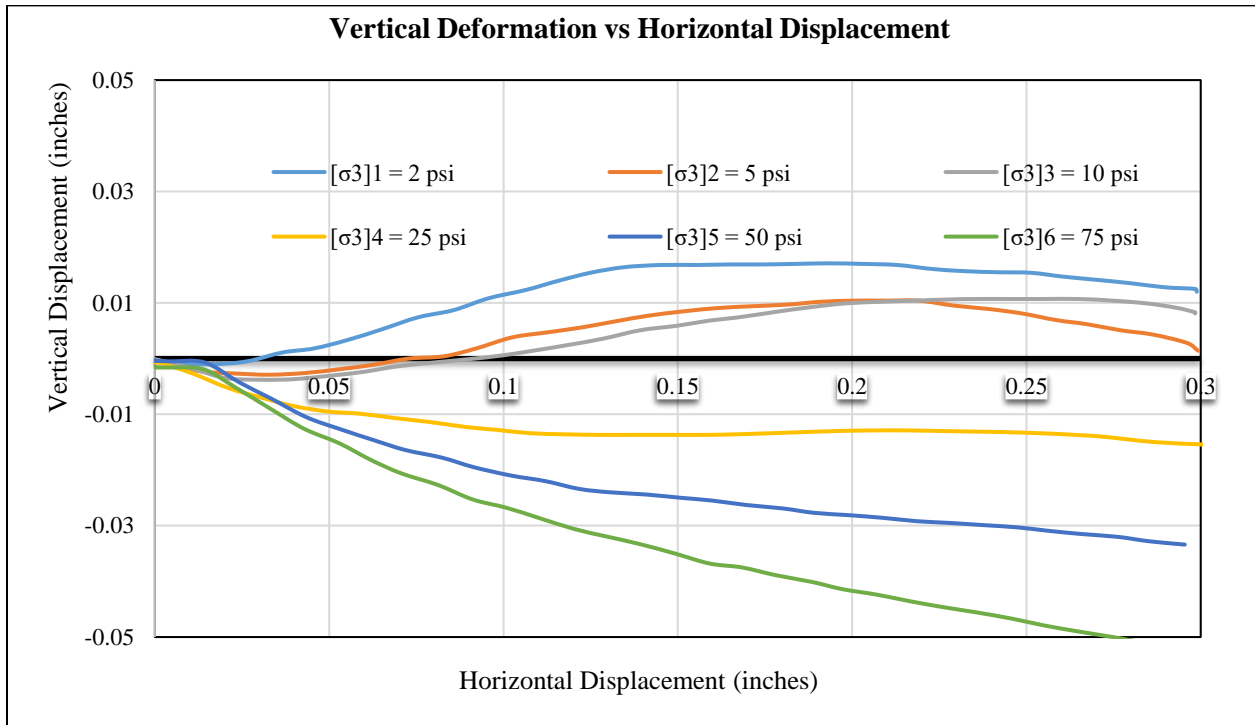


Figure 31. Vertical deformation vs. horizontal displacement relationship for RC=83.6%, SR=7.62 mm/min.

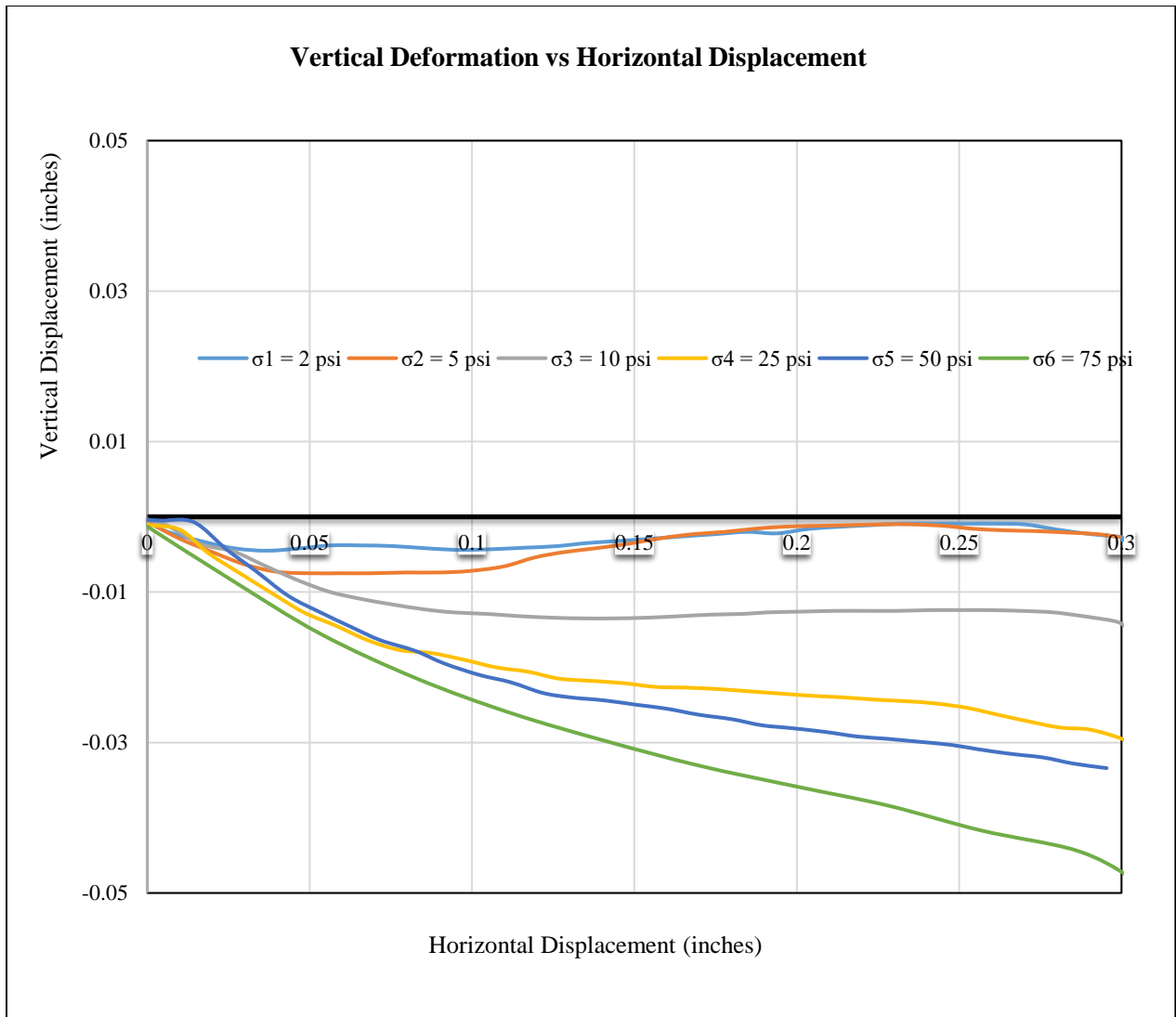


Figure 33. Vertical deformation vs. horizontal displacement relationship for RC=75.4%, SR=7.62 mm/min.

Each curve in Figures 29-33 tends to exhibit a dilation behavior with the application of normal and shear stresses as the initial relative compaction values increases. Figure 34 provides an overall representation of the dilation (Ψ^0) behavior of JSC Mars-1 subjected to the combination of normal and shear stresses for a range of initial relative compaction (RD , %) and deformation rates (SR , mm/min).

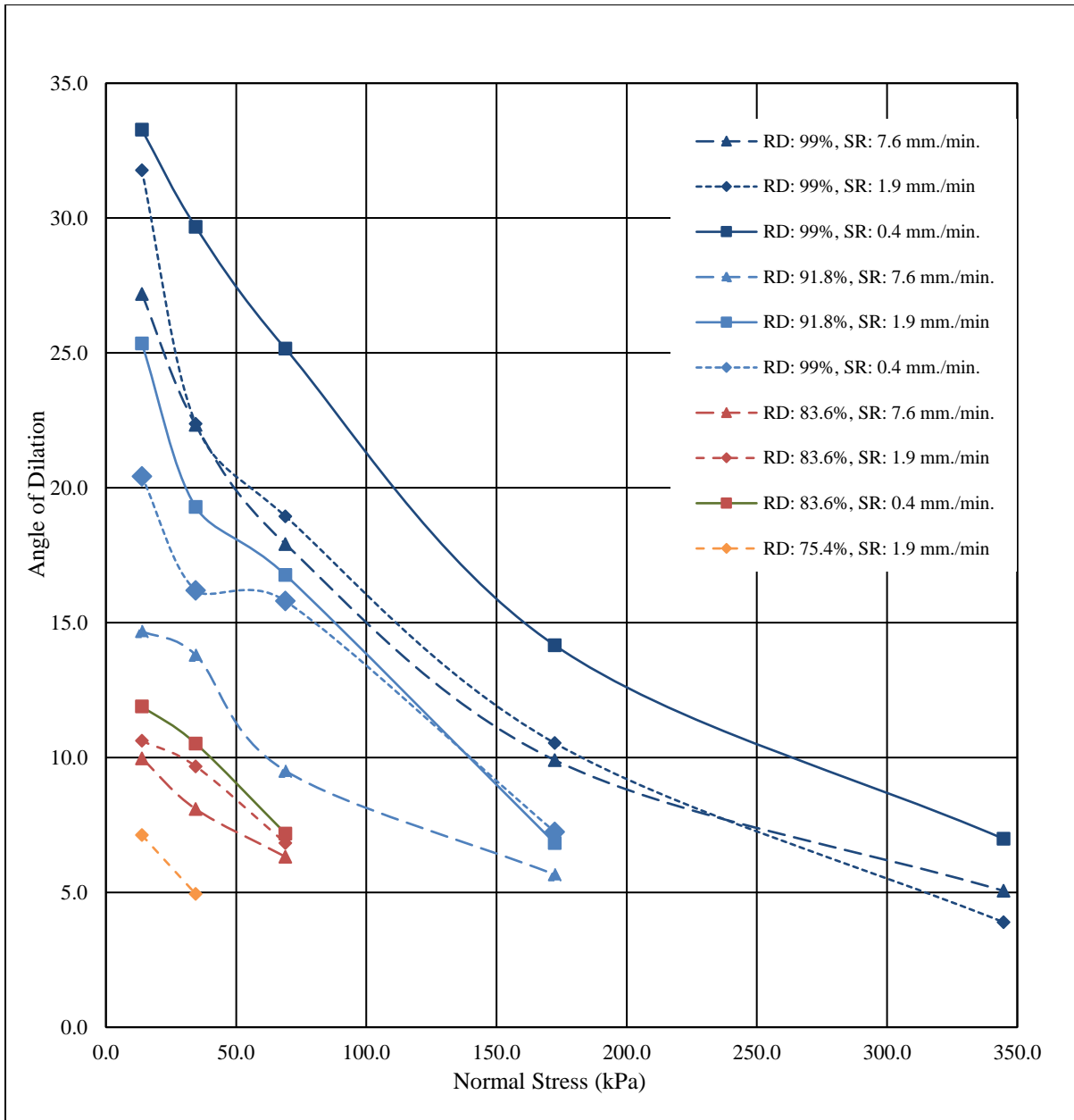


Figure 34. Angle of dilation vs. normal stress (kPa).

JSC Mars-1 specimens with high initial density exhibit a high angle of dilation (Figure 34). As such, specimens with low density experience densification while the triaxial loads are applied during the test. In addition, the angle of dilation for JSC Mars-1 tends to increase as the strain rate decreases (Figure 34). A summary of the calculated angles of dilation (Ψ^{θ}) is given in Table 17

Table 17. Direct Shear Test: Angles of Dilation

	RC: 99.0%		RC: 91.8%		RC: 83.6%		RC: 75.4%	
SR	Normal Stress (kPa)	(Ψ°)	Normal Stress (kPa)	(Ψ°)	Normal Stress (kPa)	(Ψ°)	Normal Stress (kPa)	(Ψ°)
7.6	13.8	27.2	13.8	14.7	13.8	10.0	13.8	0.0
	34.5	22.3	34.5	13.8	34.5	8.1	34.5	0.0
	68.9	17.9	68.9	9.5	68.9	6.3	68.9	0.0
	172.4	9.9	172.4	5.7	172.4	-	172.4	-
	344.7	5.1	344.7	-	344.7	-	344.7	-
1.9	13.8	31.8	13.8	25.3	13.8	10.6	13.8	7.1
	34.5	22.4	34.5	19.3	34.5	9.7	34.5	4.9
	68.9	18.9	68.9	16.8	68.9	6.8	68.9	-
	172.4	10.5	172.4	6.8	172.4	-	172.4	-
	344.7	3.9	344.7	-	344.7	-	344.7	-
0.4	13.8	33.3	13.8	20.4	13.8	11.9	13.8	8.1
	34.5	29.7	34.5	16.2	34.5	10.5	34.5	7.9
	68.9	25.2	68.9	15.8	68.9	7.2	68.9	6.2
	172.4	14.2	172.4	7.2	172.4	-	172.4	-
	344.7	7.0	344.7	-	344.7	-	344.7	-

CHAPTER 8: IMPACT OF PARTICLE MORPHOLOGY

The purpose of this chapter is to analyze the role that soil mineralogy and particle morphology plays in the performance of soil materials. Crushed aggregate limestone material was sampled in a local quarry at El Paso, Texas. The material was sieved to replicate the gradation parameters of JSC Mars-1. For the purposes of this study, we name this new simulant as EP-Limestone. A series of 78 direct shear tests and one-dimensional compressibility test were conducted to determine the mechanical properties of JSC Mars-1 mechanical properties associated with particle's crushing behavior and morphology. The purpose of this chapter is to provide a comparison of the mechanical properties of both materials, JSC Mars-1 and EP-Limestone.

8.1 Development of EP-Limestone as an Alternative Simulant

The development of EP-Limestone as a simulant consisted of the replication of the particle-size distribution curve developed for JSC Mars-1 (Figure 5). Other physical properties, such as specific gravity, particle morphology, and particle geometry, were compared for the purposes of the comparisons to be done between JSC Mars-1 and EP-Limestone.

The raw material for El Paso Limestone was provided by Jobe Materials, L.P., a local aggregate supplier with a limestone quarry in Avispa Canyon, Texas. The geological unit corresponding with this location is the Hueco Limestone (Harbour, 1972). The middle unit of the Hueco Limestone consist of 67% of limestone, which is completely exposed near Avispa Canyon. (Harbour, 1972). The material collected at the quarry at Avispa Canyon was dry and wet sieved (Figure 36). Each particle size group was separated and remixed to conform to the same concentration as in JSC Mars-1 (Figure 5). The purpose of wet sieving the material is to eliminate excess fine-grained particles. The wet sieving operation was repeated until the wash water was clear. The purpose of dry sieving is to separate the coarse-grained particles by size.

A Mohr-Coulomb Failure envelope and a compression curve were plotted for EP-Limestone so that a preliminary comparison with JSC Mars-1 could be done. It was noted that the material exhibited high cohesion and compressibility index values respect to JSC Mars-1 (Figure 35). This is due to the excessive amount of fine-grained particles that cannot be removed by dry sieving alone. For this reason, the wet sieving was decided to be implemented. Figure 35 provides a side-by-side comparison of the mechanical properties of EP-Limestone developed by both wet and dry sieving.

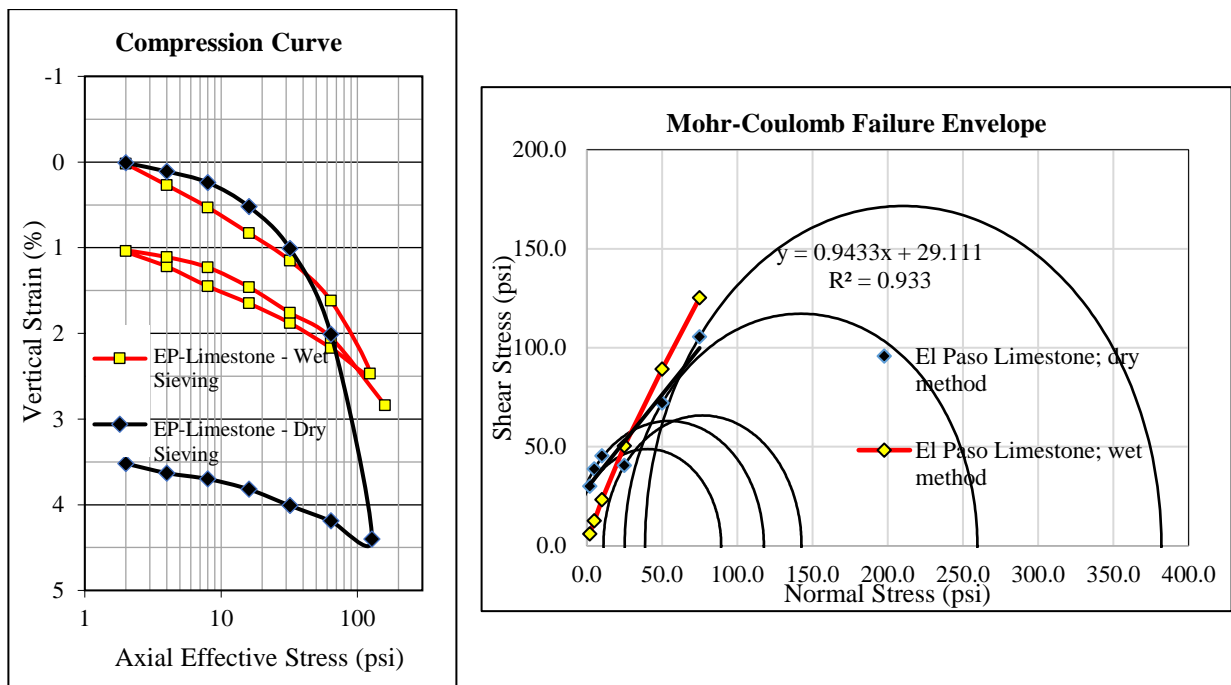


Figure 35. Influence of wet sieving on mechanical properties of EP-Limestone. (Left) Compression curves obtained from wet and dry sieving. (Right) Mohr-Coulomb failure envelopes obtained from wet and dry sieving.

As shown in Figure 35, the excessive concentration of fine-grained material has a negative impact in the performance of EP-Limestone. The pre-compression pressure tends to decrease, whereas the slope of the virgin curve tends to be increase as a function of fines concentration. Furthermore, the Mohr-Coulomb failure envelope shows an increase in the cohesion strength and a decrease in the angle of internal friction as a function of fines concentration. These behaviors are

directly associated with the presence of excess fine-grained particles that can only be removed by wet sieving methods.



Figure 36. Dry (left) and wet (center) sieving of EP-Limestone particles. (Right) Sieved material.

8.2 JSC Mars-1 vs EP-Limestone: Physical Properties

As shown in Table 5, the chemical composition of JSC Mars-1 consists mostly of silica, (SiO_2), 34.5%; alumina (Al_2O_3), 18.5%; and ferric oxide (Fe_2O_3), 12.4%. Aggregates with these chemical properties tend to exhibit a higher behavior of particle breakage when compared to limestone aggregates. As demonstrated in Section 6.4, JSC Mars-1 exhibits low resistance to load applications due to degradation.

Another point of comparison of JSC Mars-1 and EP-Limestone is specific gravity. A series of tests were performed on both JSC Mars-1 and EP-Limestone in accordance with ASTM D854 to determine their specific gravities. The specific gravity values obtained for JSC Mars-1 and EP-Limestone are 2.63 and 2.72, respectively (Figure 37). The difference of the specific gravity values

and the angularity indices of both materials (Section 8.3), represents an impact in the mechanical properties of EP-Limestone (Section 8.4).

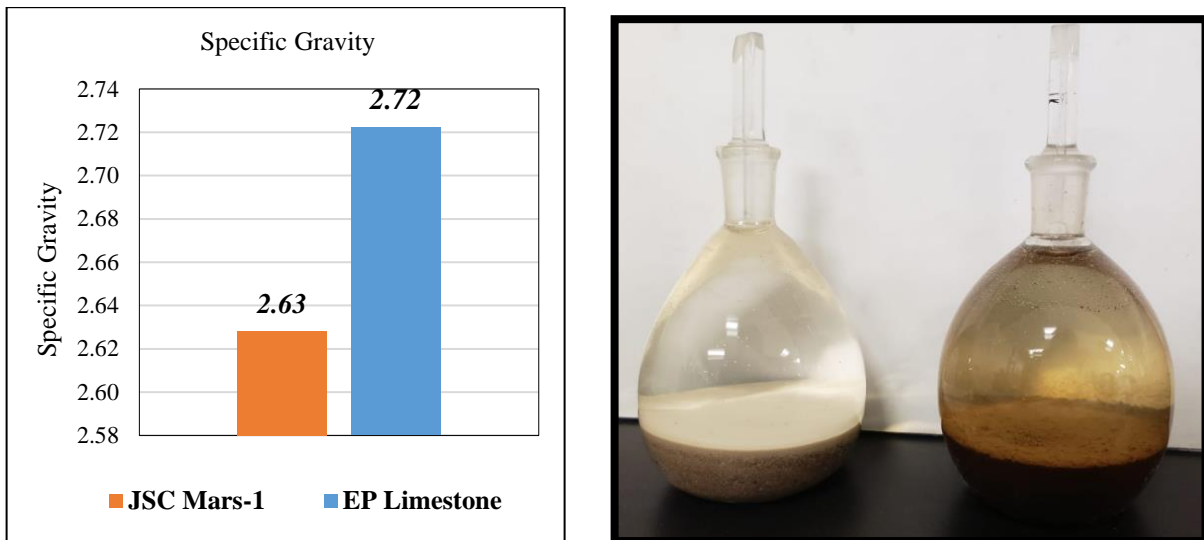


Figure 37. (Left) Specific gravity of JSC Mars-1 and EP-Limestone. (Right) Pycnometers containing EP-Limestone and JSC Mars-1 materials.

8.3 JSC Mars-1 vs EP Limestone: Particle Morphology

The angularity index of EP-Limestone is generally lower than that of JSC Mars-1. As shown in Figure 21, JSC Mars-1 has a higher concentration of particles in the size range 0.60-0.30 mm that falls in the range of moderate- to extreme-angularity index. By comparison, EP-Limestone has a higher angularity index for smaller particle sizes in the range 0.15-0.075 mm. The high values of the angularity index for the smaller particles of EP-Limestone, in addition to the particle crushing behavior, are important to be considered when comparing the mechanical performance of JSC Mars-1 and EP-Limestone, especially in terms of angle of internal friction.

As discussed in Chapter 7, angle of internal friction is a soil mechanical property that is dependent on several parameters, including density, angularity index, and concentration of coarse-grained particles. In the same way, particle strength, or resistance to degradation, is also an important parameter that influences the angularity index, the density, and the concentration of

coarse-grained particles, especially under the application of dynamic loads (Yoshimoto et al., 2012).

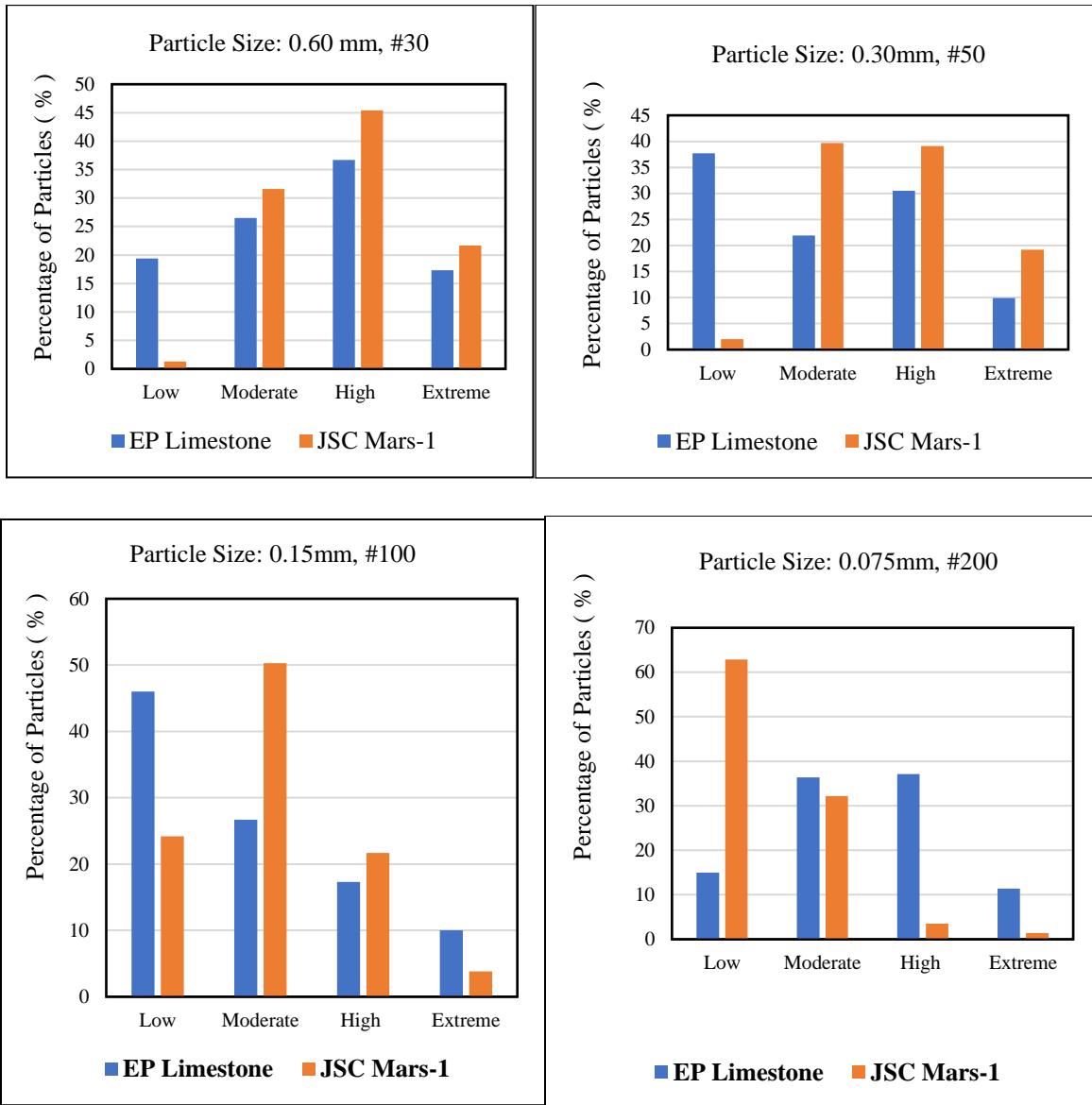


Figure 38. Angularity indices of JSC Mars-1 and EP-Limestone for various particles sizes.

As shown in Figure 38, the moderate, high, and extreme angularity index values are higher for the #30 and #50 JSC Mars-1 particles than they are for EP-Limestone. These particles, which correspond to the coarse-grained size fraction, are the governing ones in terms of friction and therefore, shear strength.

The angularity index values of JSC Mars-1, which depend on the fine-grained particles (#100 and #200), tend to be lower compared to the angularity index values of EP-Limestone. Given that, as described in Section 6.4, the coarse-grained particles of JSC Mars-1 tend to exhibit degradation. The angularity index is also affected by the generation of fine-grained particles with low angularity index values.

8.4.1 COMPRESSIBILITY

The purpose of this section is to compare of the mechanical properties of JSC Mars-1 and EP-Limestone. For this, a set of one-dimensional compression curves were developed for EP-Limestone. The same procedures and input parameters were applied as Section 7.2.

As shown in Figure 39, the compressibility values of JSC Mars-1 are more dependent to axial load at low relative compaction values. In contrast, EP-Limestone exhibits less dependency at the same conditions. On the other hand, the JSC Mars-1 and EP-Limestone one-dimensional compression curves do not differ from one another for high values of initial relative compaction. The main difference between these two scenarios is that the particle crushing behavior of JSC Mars-1 starts to take place before the load application phase of the test. As a matter of fact, and as demonstrated by Section 6.5, the generation of fines for JSC Mars-1 occurred during the compaction phase of the specimen to achieve the 99% of initial relative density before the actual compression test.

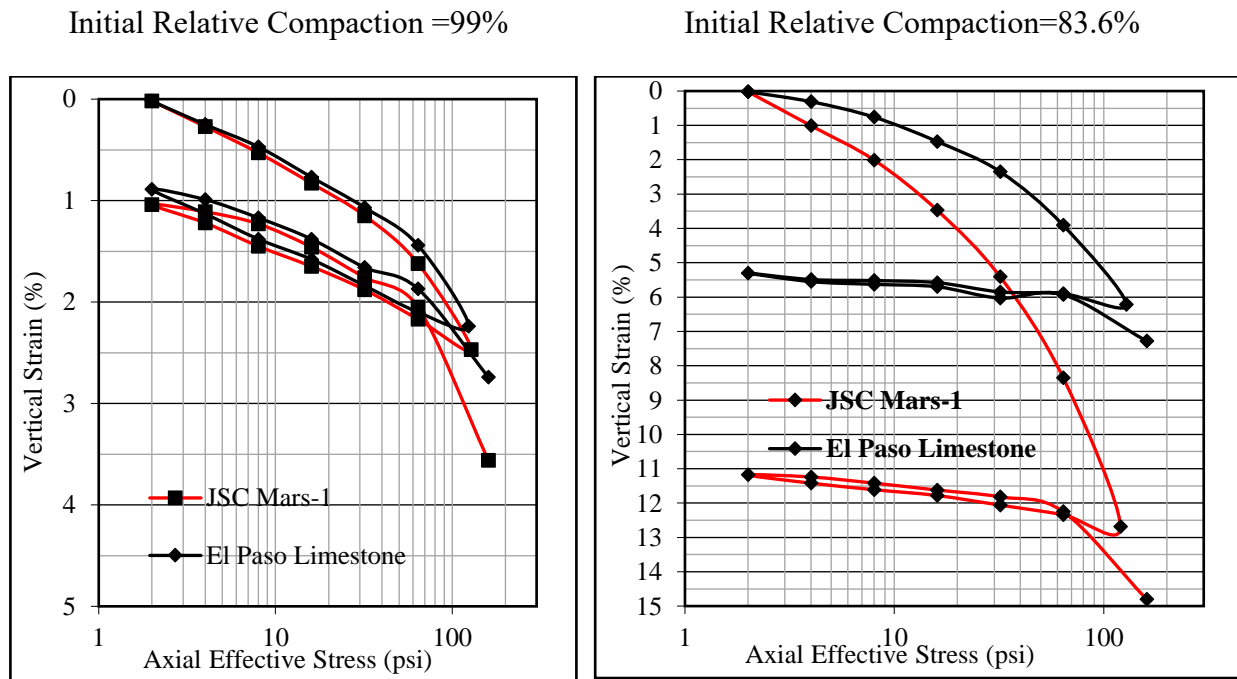


Figure 39. One-dimensional compression curves for JSC Mars-1 and EP-Limestone for relative initial compaction of 99% (left) and 83.6% (right).

8.5.2 SHEAR STRENGTH

The shear strength properties of JSC Mars-1 were also compared with those of EP-Limestone. An additional set of 72 direct shear tests were conducted with EP-Limestone material with the same input parameters described in Table 15. The computed Mohr-Coulomb failure envelopes were used to calculate the angle of internal friction, cohesion, and shear strength properties of EP-Limestone (ASTM D3080). Figures 40 and 41 compare the measured cohesive and frictional properties of JSC Mars-1 with those of EP-Limestone.

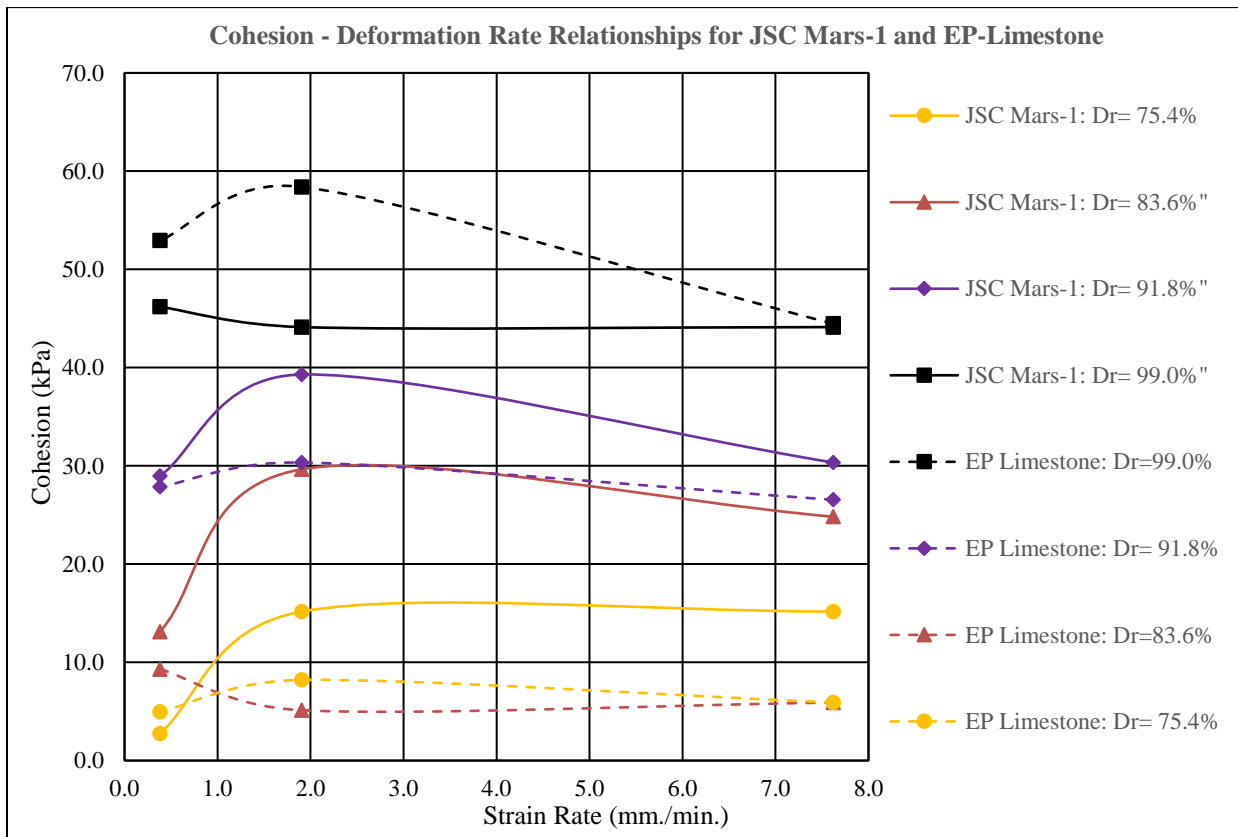


Figure 40. Comparison of the cohesion properties of JSC Mars-1 and EP-Limestone.

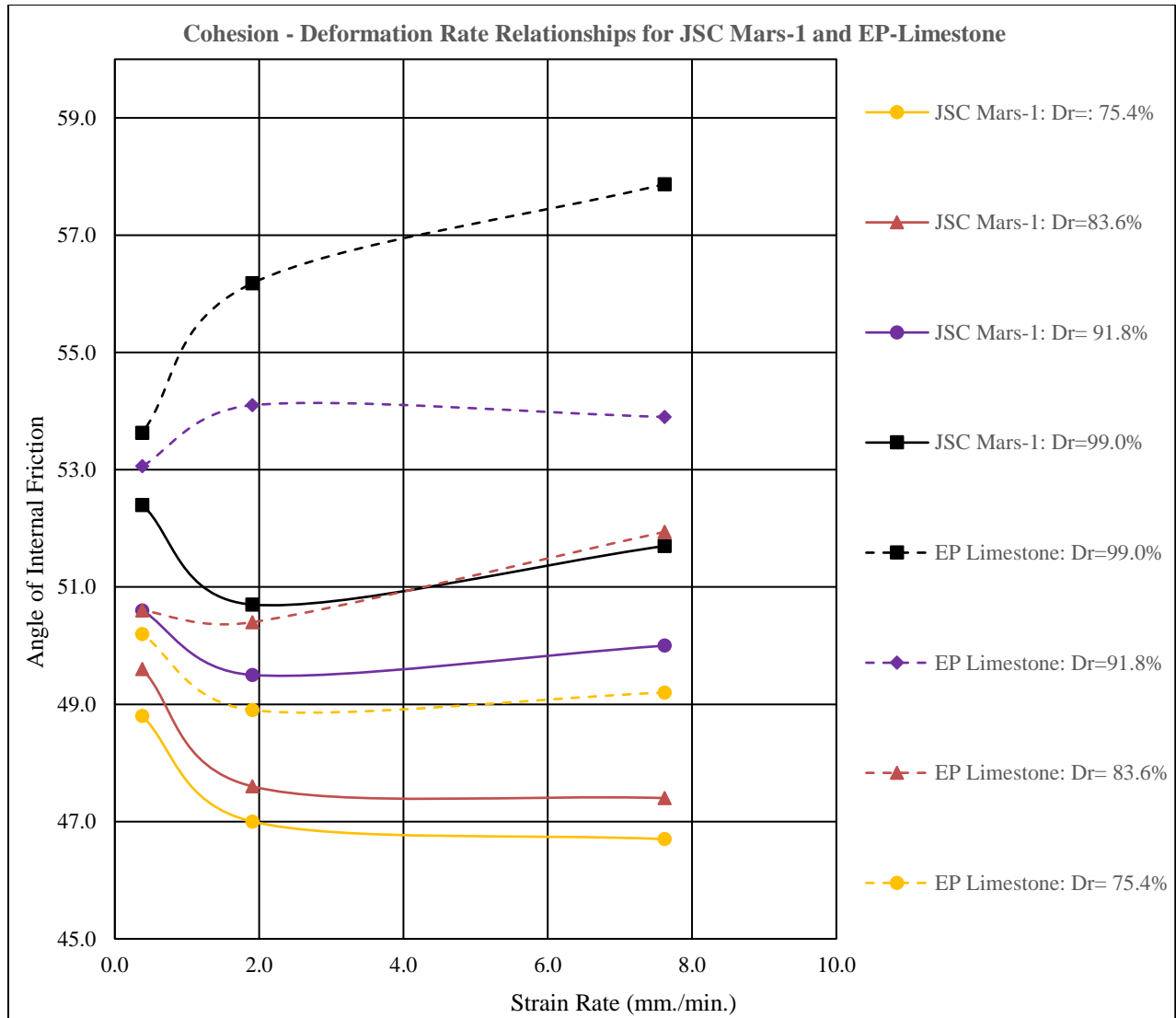


Figure 41. Comparison of the angle of internal friction of JSC Mars-1 and EP-Limestone.

As shown in Figures 40 and 241, EP-Limestone exhibits better performance under triaxial loading than JSC Mars-1. Strength relationships for both cohesion and angle of internal friction parameters present a similar behavior, except that curves corresponding to EP-Limestone are clearly shifted upwards with respect to those for JSC Mars-1 (Figure 41). As stated at the beginning of this chapter, soil mineralogy plays a significant role in the degradation behavior of granular materials that consequently, affect mechanical properties. This is the reason for the larger gap

between the angles of internal friction curves resulting from tests of both materials at high relative density values.

At high relative densities, materials with high particle breakage are more susceptible to be affected by secondary compression (Ghafghazi et al., 2014). Secondary compression occurs after the air and/or water pore pressure is fully dissipated. At that point, particle breakage takes place and the settlement process continues. Since, at low relative density conditions, the effective stresses are lower when compared with specimens with high density values, particles are less susceptible to be crushed against each other. Therefore, the gaps between the JSC Mars-1 and EP-Limestone curves are smaller compared to curves plotted for higher densities.

8.5.3 DILATANCY BEHAVIOR

The study of the variability in the dilatancy behavior between JSC Mars-1 and EP-Limestone supports the observations established in Section 8.3. Figure 42 provides a side-by-side comparison of the angles of dilation calculated by the parameters obtained from the direct shear tests. Angles of dilation at low normal stresses are generally higher for JSC Mars-1 compared to EP-Limestone. Since coarse-grained particles in JSC Mars-1 exhibit a higher angularity index in comparison to EP-limestone, it is logical to conclude that dilation is higher for JSC Mars-1 due to the particle interlocking effect. However, this behavior is only effective at low normal stress values. In contrast, as the normal stress increases, the slope of the dilation relationship is reduced for EP-Limestone, compared to the steep slopes corresponding to JSC Mars-1 curves (Figure 42). Eventually, no dilation occurs for JSC Mars-1 when subjected to normal loads greater than 344.7 kPa (Figure 42). A possible explanation for this is that the particle crushing behavior of JSC Mars-1 occurs at high levels of confinement (see Section 6.4). Angularity properties of soil particles are

reduced when degradation occurs, affecting the dilation behavior of specimens subjected to shear and normal stresses.

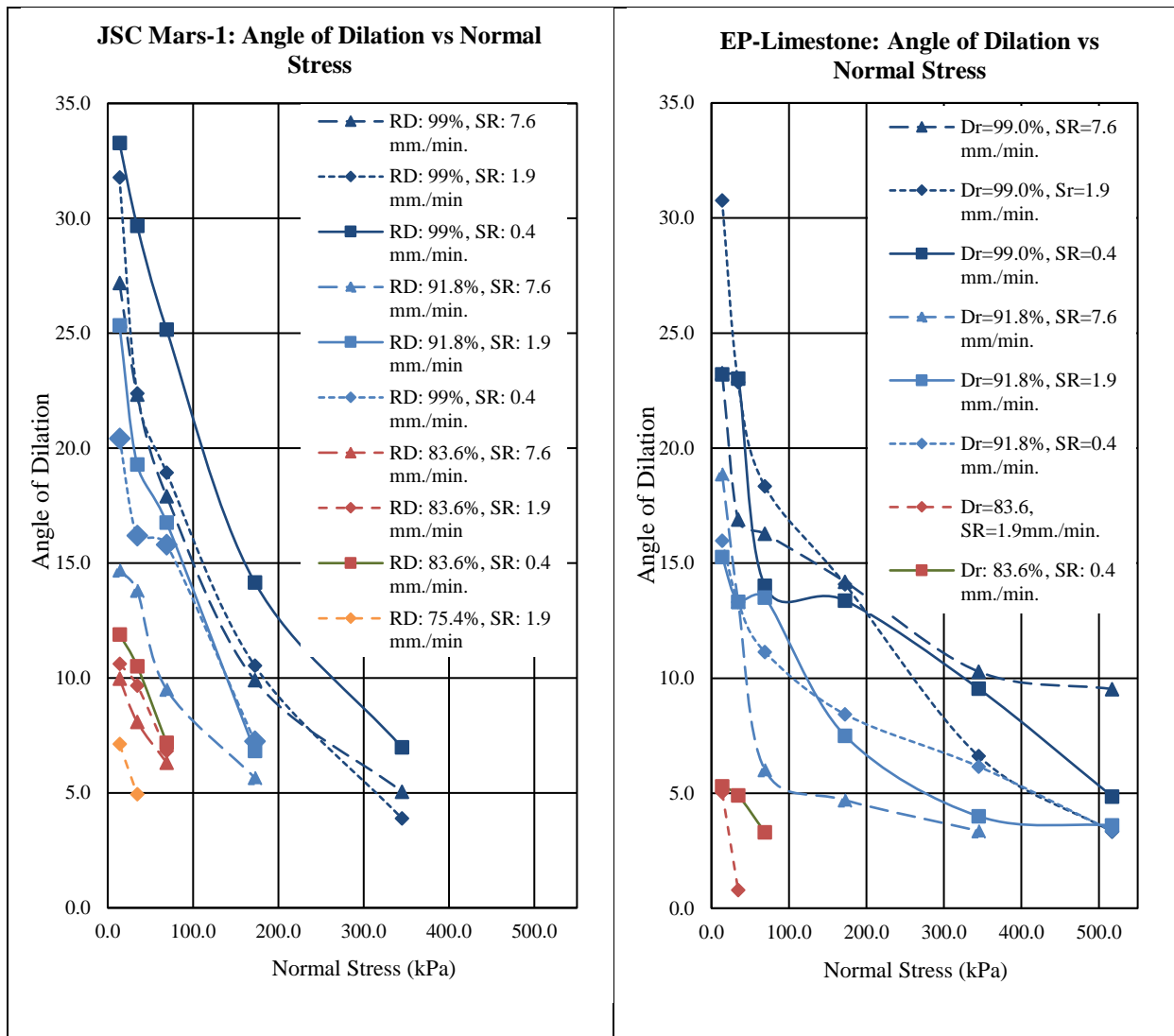


Figure 42. Dilation behavior of JSC Mars-1 (left) compared to EP-Limestone (right).

In conclusion, the high angularity index exhibited by JSC Mars-1 results in a higher angle of dilation with respect to the EP-Limestone, but only at low levels of confinement (Figure 42). Whereas, the particle crushing behavior associated with the mineralogy of JSC Mars-1 resulted in low angles of dilation at intermediate and high normal stresses, no dilation at a level of confinement of 517.1 kPa is observed for EP-Limestone (Figure 42).

CHAPTER 9: CONCLUSIONS

9.1 Key Findings

In total, 345 tests were performed to determine the physical properties of JSC Mars-1 and the variability of its mechanical properties depending on several input parameters. The testing program to characterize the JSC Mars-1 regolith simulant was based on its index and physical properties and indicated that this material can be classified as a poorly graded sand with silt (SP-SM) in accordance with the Unified Soil Classification System (USCS). Particle morphology, as determined by aggregate imaging system (AIMS), of the particles indicates high angularity index that was substantially higher compared to typical terrestrial aggregates in geotechnical practice.

JSC Mars-1 has a high angle of internal friction due to the high angularity index of the coarse-grained particles. In addition, strength tests revealed that the cohesion component of the strength of JSC Mars-1 was relatively small. However, the angle of internal friction was high at all strain-rate levels. The dilation angle of JSC Mars-1 is relatively high which implies significant nonlinearity in responses upon loading and unloading scenarios, such as passage of roving exploration vehicles operating on the surface of Mars.

This investigation demonstrates the importance of the compaction of martian regolith to enhance its strength properties. For future work, different values of the strength properties obtained in this can be used depending on the expected loading conditions, such as; the rate of deformation, and the amount and time of the appliance. Several techniques were explored to achieve the highest density and the required compaction effort. As discussed in Chapter 6, the highest dry density value for was of $1,158.2 \pm 16.0 \text{ kg m}^{-3}$

The particle crushing behavior has also been explored when subjected to different techniques for levels of compaction energy. The impact the mineralogy of JSC Mars-1 has on its

performance was contrasted with terrestrial soils to determine the durability of the regolith when subjected to triaxial loading. This is important to highlight, especially if the regolith is to be used for construction purposes.

9.2 Recommendations for Future Work

This thesis provides a complete characterization of the geotechnical aspects of the JSC Mars-1 regolith simulant. The characterization of the mechanical properties of JSC Mars-1 accounts for a wide variety of loading scenarios and *in-situ* conditions. These properties can represent, at least, the upper stratum of the Viking 1, Viking 2, and Pathfinder landing sites (Section 2.1). Based on the key findings of this thesis, the following are recommendations for future work:

1. Numerical Analysis: By using advanced simulation techniques and knowledge of the physics of particulate media, computer-simulated models of the influence that rovers and other human-made structures have on regolith can be developed. Furthermore, a sensitivity analysis of the simulant characterized in the laboratory can be developed to account for the results of particles suspended in the air, settling time of air particles, compaction, and strain and shear stresses in a low gravitational environment.
2. Image Analysis of Rover Tracks: The images captured by Mars's rovers can potentially be used to model the mechanical performance of the Martian surface under dynamic loads. Parameters to include surface trafficability, modulus of subgrade reaction, and dynamic shear modulus can be estimated based on image analysis. The laboratory testing results can be used to back-calculate the actual field properties.

3. Image Analysis of Slope Failures and other Local Soil Distresses: The mechanical properties of JSC Mars-1 presented in this thesis can be used to model landforms produced by land sliding, impact cratering, and other processes on the surface of Mars using both numerical and image analysis.

REFERENCES

- Arabali, P., Lee, S. I., Sebesta, S., Sakhaeifar, M. S., & Lytton, R. L. (2018). Application of Superpave Gyrotory Compactor for Laboratory Compaction of Unbound Granular Materials. *International Conference on Transportation and Development 2018*. doi:10.1061/9780784481554.037
- Arcement, B. J., and Wright, S. G. (2001). EVALUATION OF LABORATORY COMPACTION PROCEDURES FOR SPECIFICATION OF DENSITIES FOR COMPACTING FINE SANDS. Austin.
- Arvidson, R. E., DeGrosse, P., Grotzinger, J. P., Heverly, M. C., Shechet, J., Moreland, S. J., Newby, M. A., Stein, N., Steffy, A. C., Zhou, F., Zastrow, A. M., Vasavada, A. R., Fraeman, A. A., and Stilly, E. K. (2017). “Relating geologic units and mobility system kinematics contributing to Curiosity wheel damage at Gale Crater, Mars.” *Journal of Terramechanics*, The Authors, 73, 73–93.
- Bell, J. (2018). *The Martian Surface Composition, Mineralogy, and Physical Properties*. Cambridge Planetary Science, Cambridge University Press.
- Brian D. Prowell, E. Ray Brown, & Mike Huner. (2006, December). *EVALUATION OF THE INTERNAL ANGLE OF GYRATION OF SUPERPAVE GYRATORY COMPACTORS IN ALABAMA*. National Center of Asphalt Technology. <https://www.eng.auburn.edu/research/centers/ncat/files/technical-reports/rep03-04.pdf>. Accessed 10 April 2021
- Brown, D. (2012). NASA Rover’s First Soil Studies Help Fingerprint Martian Minerals. Nasa.

- Campbell, W. G. 1990. *Form and Style in Thesis Writing, a Manual of Style*. Chicago: The University of Chicago Press.
- Carlton C. Allen, Morris, R. V., Jager, K. M., Golden, D. C., Lindstrom, D. J., Lindstrom, M., and Lockwood, J. P. (2004). "Martian Regolith Simulant JSC Mars-1." *Lunar and Planetary Science XXIX*, (Table 2), 4–5.
- Carr, M. H., & Head, J. W. (2009, August 20). Geologic history of Mars. https://www.sciencedirect.com/science/article/pii/S0012821X09003847?casa_token=i5pBl_48oUAAAAA%3AhHoUk50ID73X3hFo7RYSmtICn3XTaFD3F0gKo2jLvaKXxPcb1rSVT8oc7ZREQ96RK_MQ1P6JEDs#bbib166. Accessed 3 May 2021
- Chen, Y.-R., & Kutter, B. L. (2009, September 15). Contraction, Dilation, and Failure of Sand in Triaxial, Torsional, and Rotational Shear Tests. *Journal of Engineering Mechanics*. American Society of Civil Engineers. [https://ascelibrary.org/doi/abs/10.1061/\(ASCE\)0733-9399\(2009\)135:10\(1155\)](https://ascelibrary.org/doi/abs/10.1061/(ASCE)0733-9399(2009)135:10(1155)). Accessed 12 April 2021
- Coles, K. S., Tanaka, K. L., and Christensen, P. R. (2019). *The Atlas of Mars*. The Atlas of Mars.
- David, L. (2014). "How Wheel Damage Affects Mars Rover Curiosity's Mission." *Space Insider*, <<https://www.space.com/26472-mars-rover-curiosity-wheel-damage.html>> (Jun. 28, 2020).
- Dhir, R. K., Brito, J. de, Lynn, C. J., & Silva, R. V. (2018). Geotechnics and Road Pavements. *Sustainable Construction Materials*, 197–237. doi:10.1016/b978-0-08-100997-0.00006-3
- Fackrell, L. E. (2018). "Development of Martian Regolith Simulants: in Situ Resource Availability and Potential ." 2018(2083), 1–2.

- Gaier, J. R. (2007). "The Effects of Lunar Dust on EVA Systems During the Apollo Missions." Nasa/Tm-2005-213610/Rev1, (March), 1–16.
- Gabasova, L. R., & Kite, E. S. (2018). Compaction and sedimentary basin analysis on Mars. *Planetary and Space Science*, 152, 86–106. doi:10.1016/j.pss.2017.12.021
- Ghafghazi, M., Shuttle, D. A., & DeJong, J. T. (2014). Particle breakage and the critical state of sand. *Soils and Foundations*, 54(3), 451–461. doi:10.1016/j.sandf.2014.04.016
- Gromov, V. (1998). "Physical and mechanical properties of lunar and planetary soils." Earth, Moon and Planets.
- GUAN, J. zhao, LIU, A. min, XIE, K. yu, SHI, Z. ning, and KUBIKOVA, B. (2020). "Preparation and characterization of Martian soil simulant NEU Mars-1." Transactions of Nonferrous Metals Society of China (English Edition), The Nonferrous Metals Society of China, 30(1), 212–222.
- Hammam, A. H., Abel-Salam, A. I., & Yousf, M. A. (2017). On the evaluation of pre-consolidation pressure of undisturbed saturated clays. *HBRC Journal*, 13(1), 47–53. doi:10.1016/j.hbrcj.2015.02.003
- Harbour, R. L. (1972). Geology of the Northern Franklin Mountains, Texas and New Mexico. doi:10.3133/b1298
- Hardin, B. O. 1985. Crushing of soil particles. *Journal of Geotechnical Engineering* 111 (10):1177–92. doi: 10.1061/(ASCE)0733-9410(1985) 111:10(1177).
- Kim, J. H., Yoon, H.-K., & Lee, J.-S. (2011). Void Ratio Estimation of Soft Soils Using Electrical Resistivity Cone Probe. *Journal of Geotechnical and Geoenvironmental Engineering*, 137(1), 86–93. doi:10.1061/(asce)gt.1943-5606.0000405

Imaging Indices for Quantification of Shape, Angularity ... Transportation Research Record
Journal of the Transportation Research Board,
www.researchgate.net/publication/269527155_Imaging_Indices_for_Quantification_of_Shape_Angularity_and_Surface_Texture_of_Aggregates.

Kaethler, S., Favier, J. J., Masson, F., and Appolloni, L. (2018). "Mars in-situ water extraction while preparing a hardened landing zone." Proceedings of the International Astronautical Congress, IAC, 2018-Octob(January 2019).

Kong, D., Chen, M., Xie, J., Zhao, M., and Yang, C. (2019). "Geometric characteristics of BOF slag coarse aggregate and its influence on asphalt concrete." *Materials*, 12(5).

Krumbein, W. C. (1941). Measurement and geological significance of shape and roundness of sedimentary particles. *Journal of Sedimentary Petrology*. Vol. 11, No. 2, pp. 64-72.

Lees, G. (1964) A new method for determining the angularity of particles. *Sedimentology*, 3, pp. 2–21.

Liu, M. D., & Carter, J. P. (1999). Virgin compression of structured soils. *Géotechnique*, 49(1), 43–57. doi:10.1680/geot.1999.49.1.43

M.E. Schmidt, C.D.K. Herd, T.J. McCoy, H. Y., and McSween, A.D. Rogers, and A. H. T. (2019). "IGNEOUS MARS: CRUST AND MANTLE EVOLUTION AS SEEN BY ROVER GEOCHEMISTRY, MARTIAN METEORITES, AND REMOTE SENSING." 50th Lunar and Planetary Science Conference 2019, 2019(2132), 5–6.

Mantovani, J. G., and Calle, C. I. (2003). "Dielectric Properties of Martian Soil Simulant." *Space Congress Proceedings*, 2(c), 56–59.

- Masad, E., Little, D., & Sukhwani, R. (2004). Sensitivity of HMA Performance to Aggregate Shape Measured Using Conventional and Image Analysis Methods. *Road Materials and Pavement Design*, 5(4), 477–498. doi:10.3166/rmpd.5.477-498
- Mitchell, J. K., David Carrier, W., Houston, W. A., Scott, R. F., Bromwell, L. G., Turan Durgunoglu, H., Hovland, H. J., Treadwell, D. D., and Costes, N. C. (1972). 8. Soil Mechanics.
- Moore, H. J., Hutton, R. E., Clow, G. D., & Spitzer, C. R. (1987). Physical properties of the surface materials at the Viking landing sites on Mars. *Professional Paper*. doi:10.3133/pp1389
- Nimmo, F., and Tanaka, K. (2005). “Early Crustal Evolution of Mars.” *Annual Review of Earth and Planetary Sciences*, 33(1), 133–161.
- “Opportunity Interactive Comparison - NASA Mars.” (n.d.).
<<https://mars.nasa.gov/mer/multimedia/interactive/>> (Jun. 28, 2020).
- Perko, H. A., Nelson, J. D., & Green, J. R. (2006). Mars Soil Mechanical Properties and Suitability of Mars Soil Simulants. *Journal of Aerospace Engineering*, 19(3), 169–176. doi:10.1061/(asce)0893-1321(2006)19:3(169)
- Poulos, S. J. (1972). *Stress-strain behaviour of soils: proceedings of the Roscoe Memorial Symposium, Cambridge University, 29-31 march, 1971*. Henley-on-Thames: G. T. Foulis & CO LTD.
- Rogers, C.D.F. and Glendinning, S. (1993). Modification of clay soils using lime. In C. a. Rogers (Ed.), *Proceeding of the Seminar held at Loughborough University on Lime Stabilization* (pp. 99-114). London: Thomas Telford.

Scott, A. N., Oze, C., Tang, Y., and O’Loughlin, A. (2017). “Development of a Martian regolith simulant for in-situ resource utilization testing.” *Acta Astronautica*, Elsevier, 131(August 2016), 45–49.

Sibille, L., Carpenter, P., Schlagheck, R., and French, R. (2006). “Lunar Regolith Simulant Materials: Recommendations for Standardization, Production, and Usage.” NASA Technical Paper, (September 2006), 142.

The Four Things You Need to Know about the GEOTECHNICAL PROPERTIES OF LUNAR SOIL. Lunar Geotechnical Institute, Sept. 2005, pdfs.semanticscholar.org/2cae/a1acc878161e1b1d69654b0a8228660a348e.pdf.

Townsend, F. C. (1972). “COMPARISONS OF VIBRATED DENSITY AND STANDARD COMPACTION TESTS ON.”

TxDOT . Tex-129-E Measuring the Resistivity of Soil Materials. Texas Department of Transportation, 2014. ftp://ftp.dot.state.tx.us/pub/txdot-info/cst/TMS/100-E_series/pdfs/soi129.pdf.

Virgil Ping, W., Yang, Z., Leonard, M., & Putcha, S. (2002). Laboratory Simulation of Field Compaction Characteristics on Sandy Soils. *Transportation Research Record: Journal of the Transportation Research Board*, 1808(1), 84–95. doi:10.3141/1808-10

Wadell, H. (1933). Sphericity and roundness of rock particles. *J. Geol.* 41, No. 3, 310–331

Watters, T. R., McGovern, P. J., and Irwin III, R. P. (2007). “Hemispheres Apart: The Crustal Dichotomy on Mars.” *Annual Review of Earth and Planetary Sciences*, 35(1), 621–652.

Williams, B.M., et al. "Properties of Lunar Soil Simulant JSC-1." *Journal of Aerospace Engineering*, www.researchgate.net/scientific-contributions/2017941075_Brian_M_Willman.

Yoshimoto, N., Hyodo, M., Nakata, Y., Orense, R. P., Hongo, T., & Ohnaka, A. (2012). Evaluation of shear strength and mechanical properties of granulated coal ash based on single particle strength. *Soils and Foundations*, 52(2), 321–334. doi:10.1016/j.sandf.2012.02.009

Zimmerman, Y. (2016). "Developing a Lightweight Martian Simulant and a Miniature."
(August).

VITA

Jesus Baca was born in El Paso, Texas and raised in Parral, Chihuahua, Mexico, where he attended Las Americas Institute for elementary, middle, and high school. He then attended South Texas College in McAllen, Texas but transferred to the University of Texas at El Paso where he obtained his Bachelor of Science in Civil Engineering in the Fall of 2019. Prior to graduation, Jesus participated in several research projects under the guidance of Dr. Reza Ashtiani. These projects include geotechnical investigations in Juarez, Mexico, and field and laboratory investigations for the Texas Department of Transportation in the Eagle Ford Shale. Immediately after graduating, Jesus enrolled in the master's graduate program in Civil Engineering at UTEP where he worked as a graduate research assistant under the mentorship of Dr. Reza Ashtiani. Parallely, Jesus has worked in the industry for more than four years at LOI ENGINEERS. He has experience in project management concerning both quality control of construction materials and geotechnical assessments.

At UTEP, Jesus primarily worked on a research project for the National Aeronautics and Space Administration (NASA). During his time at UTEP, Jesus was a Dwight D. Eisenhower Transportation fellow that granted him the ability to attend the Transportation Research Board (TRB) annual meeting in 2020. Ultimately, he is intended to complete his Master of Science in Civil Engineering in the Summer of 2021.

Contact Information: jbaca12@miners.utep.edu

This thesis was typed by Jesus Baca